NWP SAF
Numerical Weather Prediction

The EUMETSAT
Network of
Satellite Application
Facilities
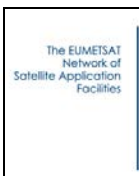
Document NWPSAF-KN-TV-009

Version 1.0

19-05-2016

ASCAT-6.25 validation

Jur Vogelzang

KNMI, De Bilt, The Netherlands

ASCAT-6.25 validation

Jur Vogelzang (KNMI)

This documentation was developed within the context of the EUMETSAT Satellite Application Facility on Numerical Weather Prediction (NWP SAF), under the Cooperation Agreement dated 29 June 2011, between EUMETSAT and the Met Office, UK, by one or more partners within the NWP SAF. The partners in the NWP SAF are the Met Office, ECMWF, KNMI and Météo France.

Change record			
Version	Date	Author / changed by	Remarks
0.1	Dec 2013	Jur Vogelzang	First draft
0.2	Aug 2014	Jur Vogelzang	Added chapters 5 and 6
0.3	May 2015	Jur Vogelzang	Added chapter 7
1.0	Jan-May 2016	Jur Vogelzang	Added introduction and conclusions; combined old chapters 3 and 4 into new chapter 3

Contents

1   Introduction

1.1   Aims and scope

For some time the ASCAT wind data processor (AWDP) offers the possibility to process data on a 6.25 km grid (ASCAT-6.25). Development of this option has been driven by user demand to higher spatial resolution. ASCAT-6.25 processing capabilities become operational in AWDP version 2.4, which will be released early 2016.

This report describes the validation of the ASCAT-6.25 product.

1.2   Introductory remarks

Chapter 2 describes in detail how the MLE and Kp normalisation tables in AWDP were adjusted to the 6.25 km grid. Some software needed is listed in appendices A to E.

Chapter 3 gives the buoy comparison for one month of ASCAT-6.25 data. Comparison with ASCAT-coastal data shows that ASCAT-6.25 deviates slightly more from the buoy winds than ASCAT-coastal (grid size 12.5 km). This is a bit surprising, since one expects that on average the ASCAT-6.25 data lie closer to the buoys than the ASCAT-coastal data, resulting in better agreement. MLE statistics and statistical consistency are shown to be comparable to those of ASCAT-coastal.

Chapter 4 studies the averaging radius used for aggregating the full resolution radar cross section data. It is shown that decreasing the aggregation radius increases a bump in the spectrum at high wavenumbers. This bump is already weakly visible in ASCAT-coastal spectra. Spatial variances show that this bump is caused by noise. The spatial variance analysis can be extended to calculate the excess noise (w.r.t. an aggregation radius of 15 km corresponding to an oversampled ASCAT-coastal product). In appendix F it is shown that not only the noise, but also its correlation coefficients can be calculated. The ASCAT-6.25 product has correlated noise, and this correlated noise causes the peculiar bump observed in the spectra. Comparison with buoy data and triple collocation show that an aggregation radius of 7.5 km for the ASCAT-6.25 product yields acceptable noise levels.

In chapter 5 it is shown that the correlation in the noise is due to overlap of the cumulative spatial response using the ASCAT spatial response code of Richard Lindsley [*Lindsley*, 2014; *Lindsley et al*., 2015]. It is also shown directly by comparing cumulative spatial responses that the ASCAT-6.25 product has better resolution than ASCAT-coastal.

In chapter 6 it is attempted to improve the spatial sampling of the full resolution radar cross sections by using elliptical aggregation areas. Though this attempt is not successful, it leads to insights along which lines improvements can be expected.

Chapter 7 gives some beta user feedback and some suggestions for further study. It also summarises the conclusions of this study. Some technical details are described in the appendices, as indicated above.

1.3 Acknowledgements

The author wishes to acknowledge the contributions from the following people:

Anton Verhoef (KNMI) who set up the procedure for calculating the K_p and MLE tables described in chapter 2;

Jeroen Verspeek (KNMI) for calculating the Numerical Ocean Calibration (NOC) corrections for ASCAT-6.25;

The beta testers M. Bourassa and A. Hazelton (Florida State University, USA), A. Horvath (Rutherford Appleton Laboratory, UK) , M. Kuzmić (Ruder Bošković Institute, Croatia), and I. Monteiro (Instituto Português do Mar e da Atmosfera, Portugal), whose feedback is reported in chapter 7;

R. Lindsley (Brigham Young University, USA) who kindly provided the software for calculating the ASCAT spatial response function (SRF) in chapter 5.

2 MLE and Kp tables

The ASCAT wind data processor, AWDP, produces output on a 6.25 km grid when given the command line option `-grid_size_0625` in combination with a full resolution L1B file (further referred to as SZF file). The SZF file should contain a 6.25 grid. This is the case for all SZF files produced by EUMETSAT and stored in the UMARF archive. The `-grid_size_0625` option further needs ECMWF GRIB files as input. The resulting wind product has 162 WVC's per row.

2.1 Construction of the Kp tables

The geophysical noises were calculated using the tables obtained from *Marcos Portabella* [REF?] on March 07 2008 (ascat_25000_geoph_kp_vs_speed_and_inc_ang.asc). For ASCAT 12.5, the geophysical noise is assumed to be half the value from the 25-km table. It is therefore logical to assume that the geophysical noises for ASCAT-6.25 are again half those of ASCAT-12.5. The ASCAT-6.25 geophysical noise table is calculated by program calc_geophys_kp.F90, see Appendix A. It is given as a function of incidence angle.

2.2 Construction of the MLE tables

The MLE tables were constructed in the same way as those for ASCAT-25, ASCAT-12.5, and ASCAT-coastal. The procedure is described in the KNMI Twiki pages, but as these are internal, the procedure will be described below in detail.

General considerations

- In the wind inversion, the CMOD5.n GMF for neutral winds was used.

- The following awdp command line options were used:

      -cmod 5n -calval -handleall -grid_size_0625.

  For some intermediate results the processing was speeded up by adding the command line options `-noamb -nowrite`.

- All WVCs with lat > 55 or lat < -55 degrees were skipped to exclude any ice contamination. See the following temporary code in module awdp_inversion. F90, subroutine invert_node.

```
! initialise
ierr = 0

! TEMPORARY CODE FOR NOC AND MLE TABLES
! set qual_sigma0 flag outside -55 - +55 degrees lat and return
if (cll%lat .gt.  55.0) then
  cll%wvc_quality%qual_sigma0 = .true.
  return
endif
if (cll%lat .lt. -55.0) then
  cll%wvc_quality%qual_sigma0 = .true.
  return
endif
! END TEMPORARY CODE
```

Step 1

- Run AWDP with standard settings (and standard code), and apply NWP Ocean Calibration (NOC) on the output.

- Initialise the NOC tables for 162 WVC's in AWDP.

Step 2

- Use a new MLE normalisation table (ascat_6250_MLE_norm_vs_wvc_162.asc) containing values of 1.0 for all WVC numbers. The table is located in genscat/ inversion.

- Consider only wind solutions with wind speed of > 4 m/s.

- Process all data and write for each wind solution the node number and the absolute value of the conedistance, see code below to be inserted in post_inversion.F90, subroutine normalise_conedist_ers_ascat.

```
v = inv_output%foundwindspeed(closest)
...

! normalise the cone distances for each solution
do isol = 1,inv_output%nr_of_windsolutions
  inv_output%conedistance_measured(isol)=inv_output%conedistance_measured(isol)/ &
                  (kp_total_norm * node_dependent_norm_factor)
enddo

! start temporary code
if (v .gt. 4.0) then
  write(34,'(I3,F8.3)') inv_input%node_nr, &
                        abs(inv_output%conedistance_measured(closest))
endif
! end temporary code
```

- From the resulting output file fort.34, calculate the mean absolute cone distance vs. node number, using the small Fortran program calc_mean_mles.F90 (see appendix B).

- This yields a new MLE normalisation table: ascat_6250_MLE_norm_vs_wvc_162. asc_step_2.

Step 3

- Repeat step 2, but with some changes.
- Use the MLE normalisation tables obtained in step 1 in the next processing.
- Use only wind solutions with wind speed of > 4 m/s and absolute MLE of <= 18.45.
- Process all data and write for each wind solution the node number and the absolute value of the conedistance, see code below to be inserted in post_inversion.F90, subroutine normalise_conedist_ers_ascat,

```
v = inv_output%foundwindspeed(closest)
...

! normalise the cone distances for each solution
do isol = 1,inv_output%nr_of_windsolutions
  inv_output%conedistance_measured(isol)=inv_output%conedistance_measured(isol)/ &
  (kp_total_norm * node_dependent_norm_factor)
enddo

! temporary code start
if (v .gt. 4.0) then
  if (abs(inv_output%conedistance_measured(closest)) .gt. 18.45) then
    write(35,'(I1)') 1
  else
    write(35,'(I1)') 0
    write(34,'(I3,F8.3)') inv_input%node_nr, &
                          abs(inv_output%conedistance_measured(closest))
  endif
endif
! temporary code end
```

- From the ratio between the number of '1' occurrences and the total number of occurrences in fort.35, the rejection rate can be computed using program calc_rejection_rate.F90 (see Appendix C).
- From the resulting output file fort.34, calculate again the mean absolute cone distance vs. node number using again program calc_mean_mles.F90.
- This yields a new MLE normalisation tables: ascat_6250_MLE_norm_vs_wvc_162. asc_step3.

Step 4

- Calculate the final MLE normalisation tables through multiplying the tables from step 2 and step 3 WVC-by-WVC using Fortran program calc_mle_ normalisation_table.F90 (see Appendix D).
- Calculate the QC threshold tables for each WVC number as 18.45 / (MLE norm from step 2) using Fortran program calc_qc_threshold.F90 (see Appendix E).

Step 5

- Run AWDP with the new MLE tables
- Check the output. If there are significant differences, go back to step 2. Otherwise the procedure has converged.
- REMOVE THE TEMPORARY CODE in awdp_inversion and post_inversion.

2.3 Results

The ASCAT-6.25 MLE tables were calculated for the period April 10, 2013 to May 09, 2013. This period was chosen because the tables for ASCAT-12.5 and ASCAT-25 were calculated for the same period, though in 2009, but for that year only the old ASCAT full resolution product was available at the time the tables were constructed. The procedure converged at the second iteration.
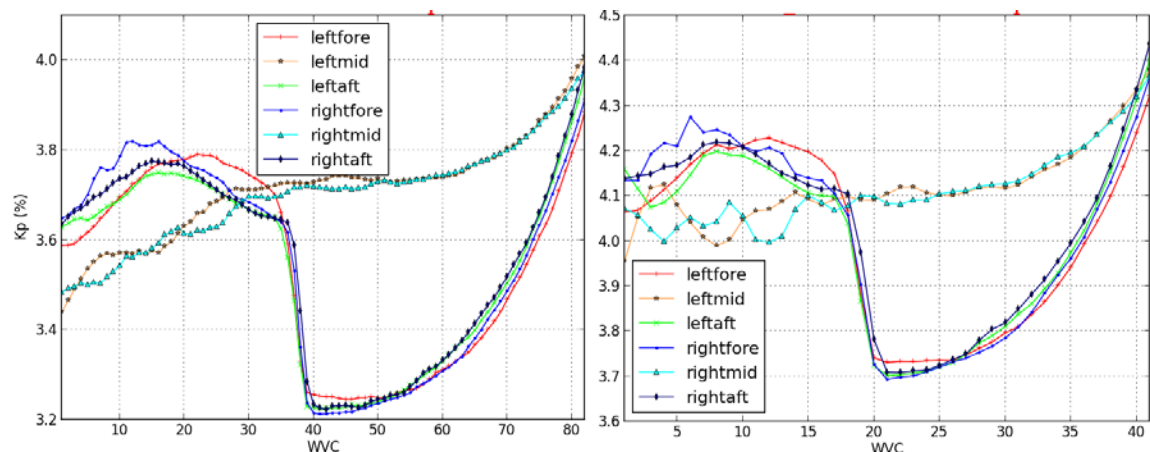
Figure 2.1   Kp value as a function of WVC number for ASCAT-6.25 (left) and ASCAT-12.5 (right). Note the difference in vertical scale

Figure 2.1 shows the average Kp value per beam for ASCAT-6.25 (left) and ASCAT-12.5 (right). Though the vertical scale differs slightly, the curves are very similar. Note that ASCAT-6.25 has a slightly lower average Kp value than ASCAT-12.5. This is due to the fact that the ASCAT-6.25 gridded radar cross sections are averaged over a smaller area. Therefore the wind variability is smaller, hence smaller Kp.

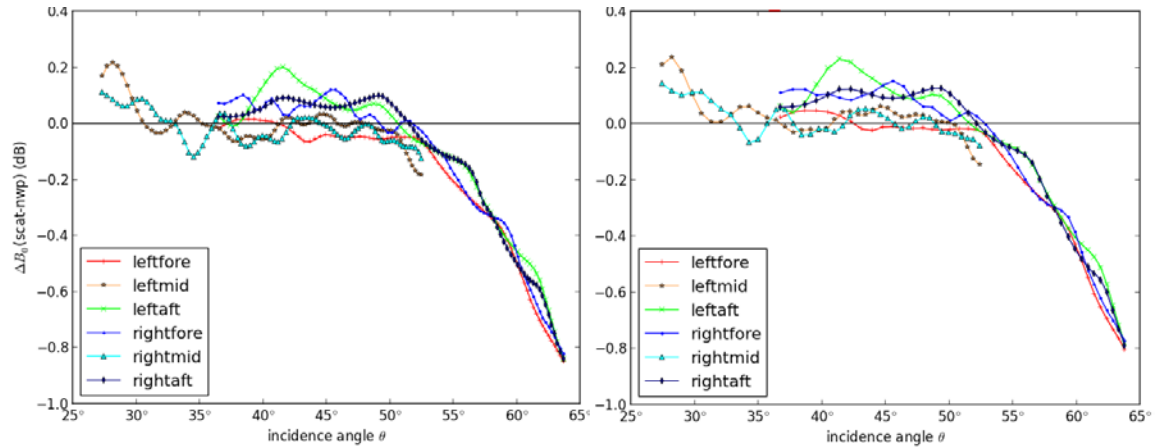**Figure 2.2** Bias per beam as a function of incidence angle for ASCAT-6.25 (left) and ASCAT-12.5 (right).

Figure 2.2 shows the bias (i.e., average difference in wind speed between scatterometer and ECMWF forecast) per beam as a function of incidence angle for ASCAT-6.25 (left) and ASCAT-12.5 (right). The biases are very similar. In particular, the wiggle pattern in ASCAT-12.5 is completely reproduced in ASCAT-6.25. This indicates that ASCAT-6.25 quality is comparable to that of ASCAT-12.5.

The rejection rates at the end of step 3 are given in table 2.1. Note that the rejection rates decrease with decreasing scatterometer grid size, but not in a linear way.

Wind product	ASCAT-6.25	ASCAT-12.5	ASCAT-25
Rejection rate	0.23%	0.28%	0.47%

Table 2.1 Rejection rates.

Note

After some time it became apparent that there was an error in the MLE normalisation tables. Apparently, the tables after step 2 in section 2.2 were taken as final normalisation. The procedure of section 2.2 was repeated for all data from August 2013 to calculate the final normalisation tables and QC rejection limits.

The ASCAT-6.25 QC rejection rate for August 2013 was 0.19%, slightly lower than the value of 0.23% for the period April-May 2013 shown in table 2.1.

Some results involving MLE statistics, notably those in sections 3.3 and 3.4, are therefore based on the MLE normalisation tables and QC threshold values of August 2013. This will be indicated in the text.

3 ASCAT-6.25 quality

3.1 *General*

Figure 3.1 shows an ASCAT scene with 6.25 km grid size (upper panel) and 12.5 km grid size (lower panel) recorded on April 10, 2013 around 02:18 UT. The wind field shows a V-shaped front east of the Kerguelen Islands with a straight southern edge and a curved northern edge. The area without wind vectors around -53 °S 73.5 °E is Heard Island and the McDonalds Islands. The front is clearly visible in the ASCAT-6.25 image, but less clear in ASCAT-12.5. Note also the difference in wind field texture: the ASCAT-6.25 wind field has a wavy texture south of the front.

The difference between the two wind fields is, of course, partly due to the fact that the ASCAT-6.25 image contains four times as many wind vectors at the same scale as the ASCAT-12.5 image. The arrows fill the image, and small changes in wind direction show up as intensity differences when looked at from some distance. Nevertheless, the ASCAT-6.25 image seems to contain more information than the ASCAT-12.5 image. The question is how to prove this.

3.2 *Buoy comparison*

Table 3.1 shows the result of the comparison of the ASCAT-6.25 and ASCAT-12.5 wind fields for the period April 10 – May 09, 2013, with collocated buoys. The buoy data were downloaded from the ECMWF archive, and only buoys not blacklisted by ECMWF were considered.

	u (m/s)		v (m/s)		speed (m/s)		dir (degrees)	
	6.25	**12.5**	**6.25**	**12.5**	**6.25**	**12.5**	**6.25**	**12.5**
bias	0.079	0.082	0.015	0.045	-0.114	-0.171	-2.018	-0.137
std dev	1.595	1.577	1.950	1.847	1.034	1.009	34.0	33.2
abs	1.022	0.998	1.228	1.173	0.768	0.764	17.3	16.7
min	-15.2	-15.1	-17.1	-17.3	-5.0	-5.4	-179.2	-179.8
max	13.1	12.6	19.6	19.6	7.4	5.7	179.3	178.1

Table 3.1 Buoy comparison.

Table 3.1 shows the following statistics: bias (average difference), standard deviation (std dev), absolute error (average absolute value of the difference; abs), minimum difference (min) and maximum difference (max). These statistics are calculated for the zonal and meridional wind components, u and v, for the wind speed and the wind direction.
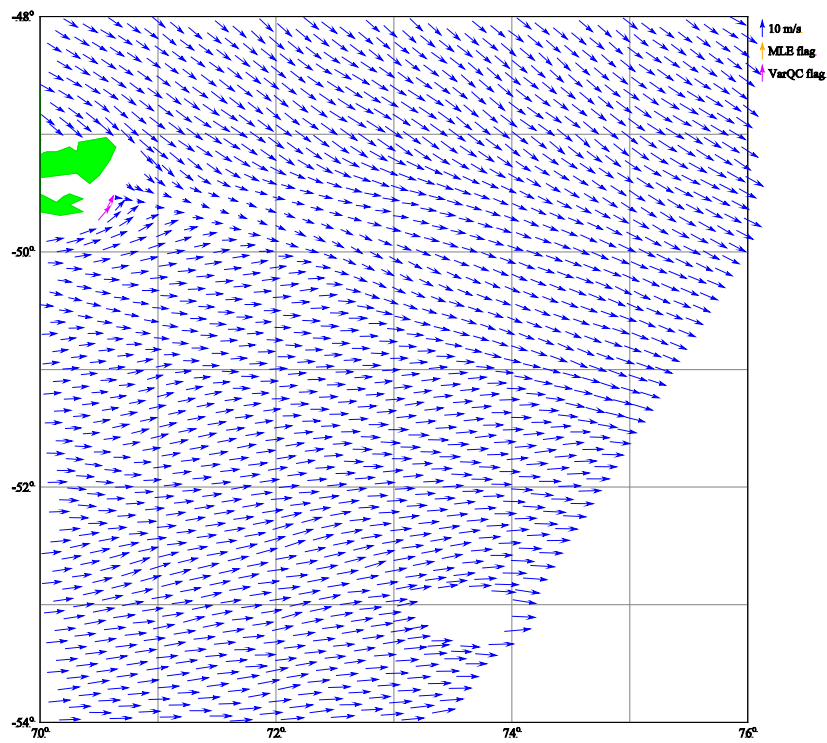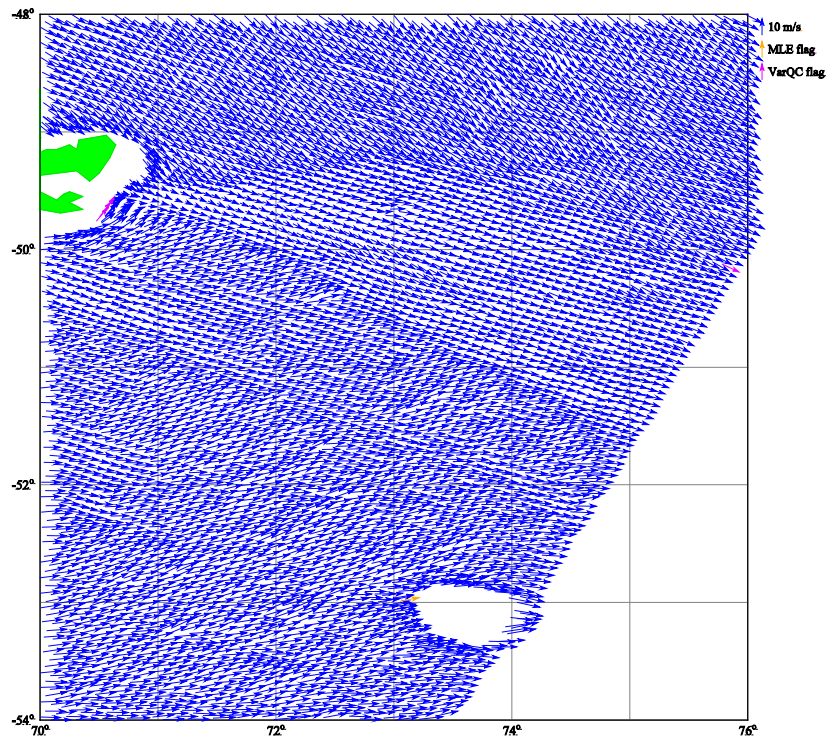
Figure 3.1 ASCAT-6.25 (upper) and ASCAT-12.5 (lower) on April 10, 2013, around 02:18 UT.

Table 3.1 shows that ASCAT-6.25 compares worse with buoys than ASCAT-12.5. The standard deviation in u is 0.02 m/s larger, that in v 0.10 m/s. ASCAT-6.25 also has a larger bias in v. The standard deviation in wind speed is comparable, but that in direction is clearly larger for ASCAT-6.25. The absolute differences behave similar to the standard deviations, indicating that the distribution of differences is not dominated by extreme values. This is supported by the minimum and maximum values that are in general slightly larger for ASCAT-6.25 than for ASCAT-12.5.

Nevertheless, it may be interesting to take a closer look at the wind fields where the extreme values occur. Figure 3.2 shows the area where the minimum difference in wind speed between ASCAT-6.25 and buoy measurements occur. The wind field is recorded on May 4, 2013, around 23:26 UT. The smallest difference of -5.0 m/s occurs at 0.04 °N, 147.01 °E, somewhere in the Tropical Pacific. Figure 3.2 shows that the scene is covered by showers, and that the point where the extreme difference occurs lies on the edge of a downdraft. Since the buoy winds are hourly averages, one may question their representativeness here.
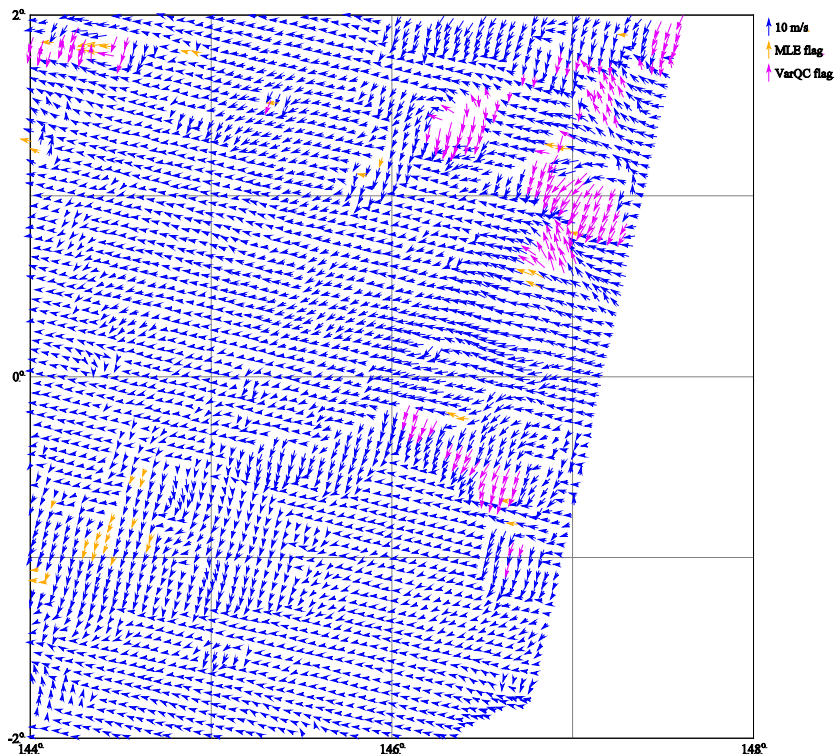

Figure 3.2 ASCAT-6.25 wind field for minimum wind speed difference with buoys, on 4 May, 2013, 23:26 UT at position 0.04 °N, 147.01 °E.
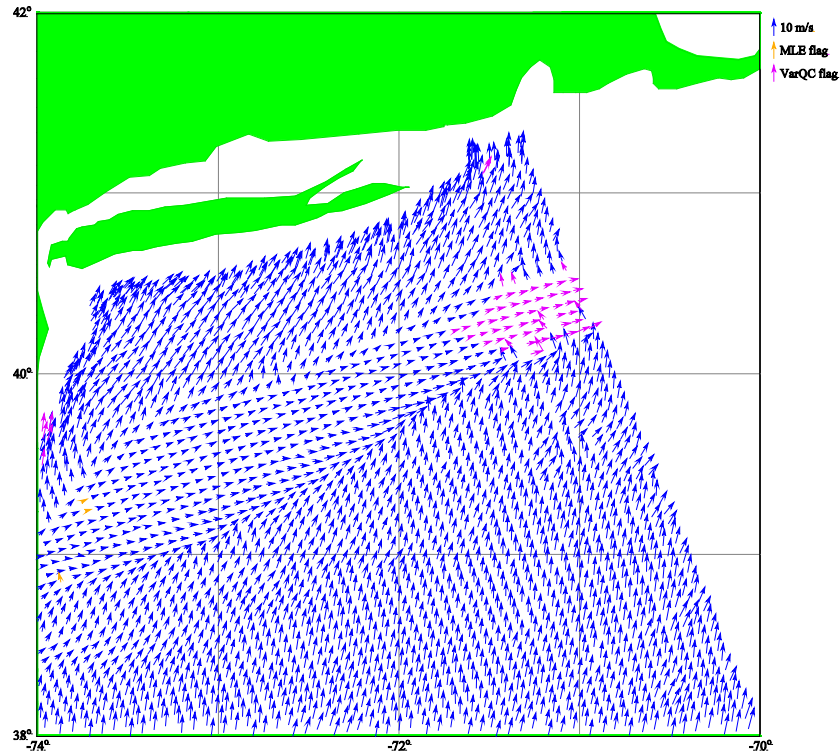
Figure 3.3   ASCAT-6.25 wind field for maximum difference in *u* and *v* with buoys, on April 13, 2013, 01:24 UT. The maximum difference in *u* occurs at position 40.17 °N, -73.22 °E, that in *v* at 40.71 °N, -71.97 °E.

Unfortunately, no buoy data in higher time resolution are available yet. These data are only in delayed mode, after the buoy hardware has been recovered, so it may take 18 months before they are available.

Figure 3.3 shows the ASCAT-6.25 wind field of April 13, 2013 around 01:24 UT close the the east coast of Canada. The wind field shows a strong convergence zone and a strong divergence zone closer to the coast, separated by a calm area with wind speeds of 3.5 to 4 m/s. The maximum difference between ASCAT-6.25 and buoy measurement in *u* equals 13.1 m/s and occurs at position 40.17 °N, -73.22 °E, right in the divergence zone. The maximum difference in *v* equals 19.6 m/s and occurs at 40.71 °N, -71.07 °E, close to the coast.
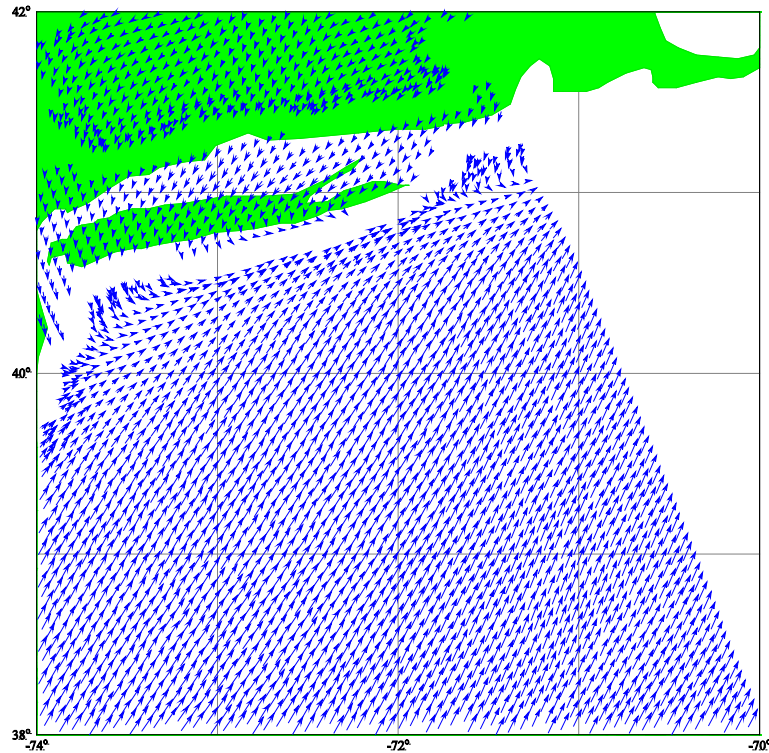
Figure 3.4 ECMWF background wind field on April 13, 2013, 01:24 UT.

The question immediately arises if the low wind structure in the ASCAT-6.25 measurements in figure 3.3 is realistic. Figure 3.4 shows the ECMWF background field. Here the structure is absent. Instead, the wind above land is blowing from the northeast, whereas on sea it is blowing from the southwest.

		max *u*				max *v*		
	ID	speed (m/s)	dir (deg)	MLE	ID	speed (m/s)	dir (deg)	MLE
Buoy	44017	11.8	30		44025	10.7	40	
ASCAT-6.25		10.0	201.1	0.00		9.5	221.1	1.40
ECMWF		5.6	231.6			5.4	226.4	

Table 3.2 Wind speed and direction for the maximum difference in *u* and *v* between ASCAT-6.25 and buoys.

Table 3.2 gives the wind speed and direction for buoy, ASCAT-6.25, and ECMWF background for the maximum difference in *u* and *v*. The table also gives the ECMWF buoy identification number and the MLE of the selected ASCAT-6.25 wind solution. As can be seen from the table, there is a large mismatch between ASCAT-6.25 and buoy wind directions. The ECMWF background direction is closer to the ASCAT-6.25 measurement, but

the ECMWF wind speed is much smaller than both buoy and ASCAT-6.25. Note that the ASCAT-6.25 measurements look reliable because of their low MLE value.

3.3 MLE statistics

Figure 3.5 shows the average MLE value as a function of wind vector cell (WVC). ASCAT-6.25 has more negative average MLE values than ASCAT-coastal. This may be due to the fact that figure 3.5 is obtained using data from August 2013, the period for which the ASCAT-6.25 MLE normalization tables were generated. Nevertheless, the differences are small and the overall variation with incidence angle is similar.
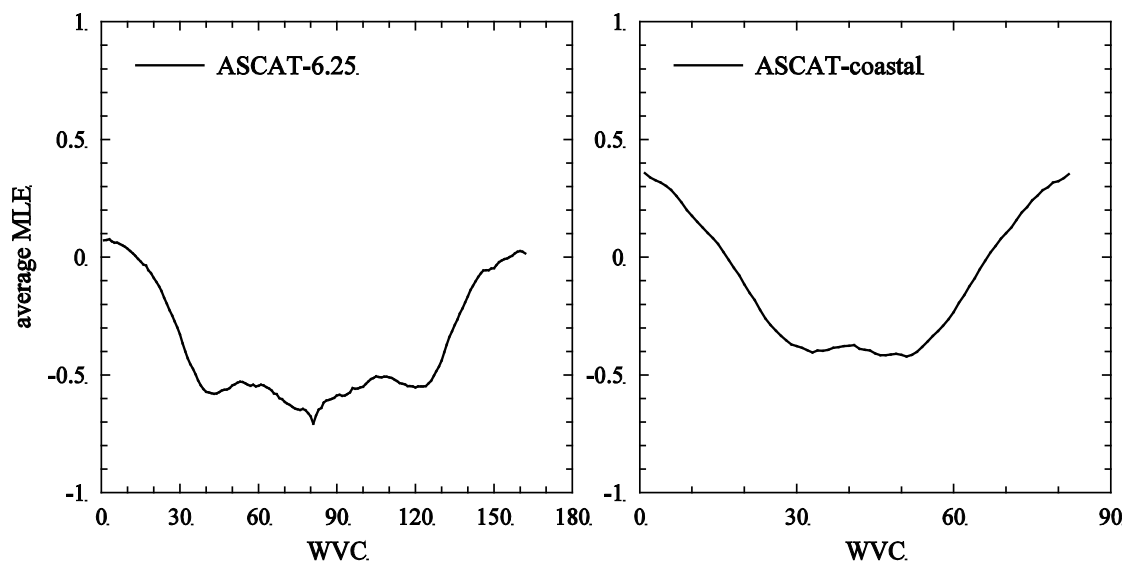
Figure 3.5 Average MLE value as a function of WVC number for ASCAT-6.25 (left) and ASCAT-12.5 (right).

3.4 Statistical consistency

The MLE value is normalized to an a-priori selection probability, p_{MLE}, for each of the ambiguities. The ASCAT-6.25 wind product is statistical consistent if the a-priori selection probability of an ambiguity is a good measure for the probability that this ambiguity is indeed selected by 2DVAR. Figure 3.6 shows the probability density function of the 2DVAR

selection probability, $p(\text{Sel})$, given that the value of p_{MLE} equals P. This is denoted as $p(\text{Sel})/p_{MLE} = P$ with P the independent variable.

The black solid curve shows the result for ASCAT-6.25, the black dashed curve for ASCAT-coastal (12.5 km grid size), based on the August 2013 data. The dotted curve gives the result for perfect statistical consistency, $p(\text{Sel})\,|\,p_{MLE} = P$ equal to $2P$.

Figure 3.6 shows that statistical consistency for ASCAT-6.25 is slightly worse than that for ASCAT-coastal. For probabilities smaller than about 0.25 it is too high, whereas for probabilities larger than about 0.75 it is too low.
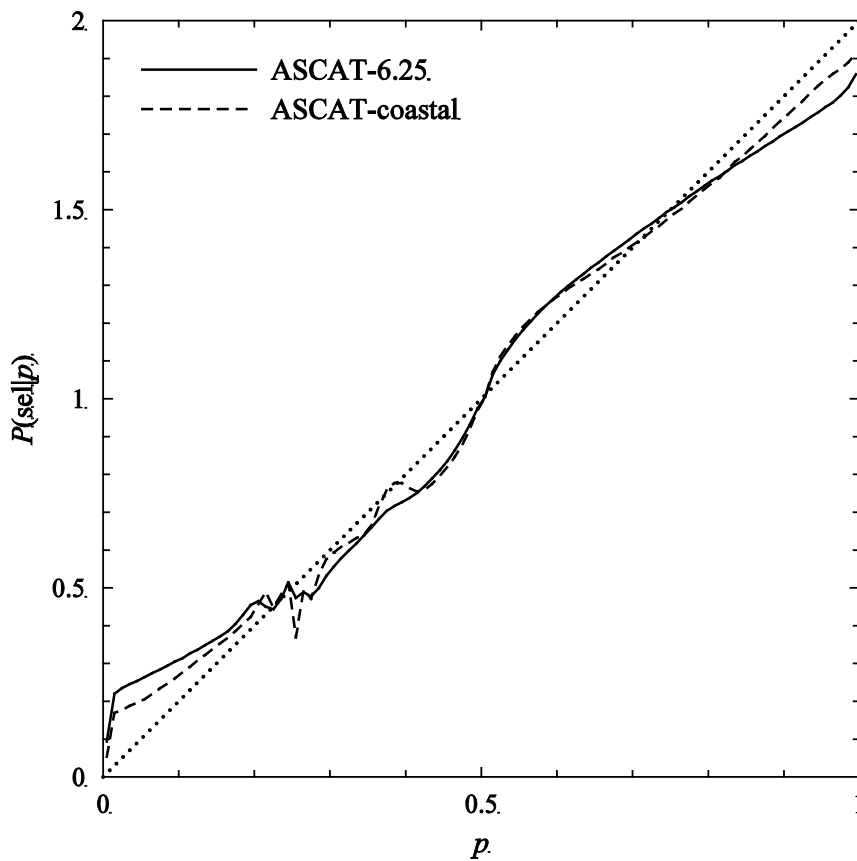

Figure 3.6 Statistical consistency (August 2013).

4   Averaging radius

4.1   Introduction

Like the ASCAT-coastal product, the cross sections per WVC for the ASCAT-6.25 product are regridded from the ASCAT full resolution L1B files using a cylindrical box average with an averaging radius R equal to 7.5 km. This is half the size of that used for the ASCAT-coastal product. This value was chosen because the ASCAT-6.25 has half the grid size of the coastal product. However, this choice is more or less arbitrary.

Decreasing the averaging radius R has as effect that less radar cross section values from the L1B product are assigned to a WVC. The resulting σ_0 value, the average of all L1B cross sections assigned to a particular WVC, is therefore more prone to measurement noise. With a larger averaging radius the noise in σ_0 is averaged out. It is clear that some optimum value must be selected for R. This optimum value may differ per application.

The ASCAT-6.25 experimental product was calculated for the periods February 2 – 13, 2012, and August 2013, using various values of the averaging radius R. In the next sections we use some popular statistics to analyse the resulting wind fields.

4.2   Spectra and autocorrelations

Figure 4.1 shows the spectra for wind components l and t for ASCAT-6.25 in the period February 2 – 13, 2012, with R equal to 5 km, 7.5 km, 10.0 km, and 15.0 km. The value of 7.5 km (dashed curves) has been used in the previous chapters. The value of 15.0 km is the same as that used for the ASCAT coastal product. Hence, these results can be regarded upon as the ASCAT-coastal product on a 6.25 km grid.

The spectra clearly develop a bump for $k \geq 10^{-5}$ m^{-1} that gets stronger when R is decreased from 15.0 km to 5.0 km. The same bump was observed earlier for the ASCAT coastal product.

In order to get more information about the origin of the bump, figure 4.2 shows the autocovariance (Fourier transform of the spectrum). However, this hardly offers any clue, though for R equal to 5.0 km a small discontinuity can be observed at small distances, indicative for measurement noise. Together with the behavior of the spectra this indicates that reducing R indeed increases the noise.

The spectra and autocorrelations for August 2013 are similar (no results shown).
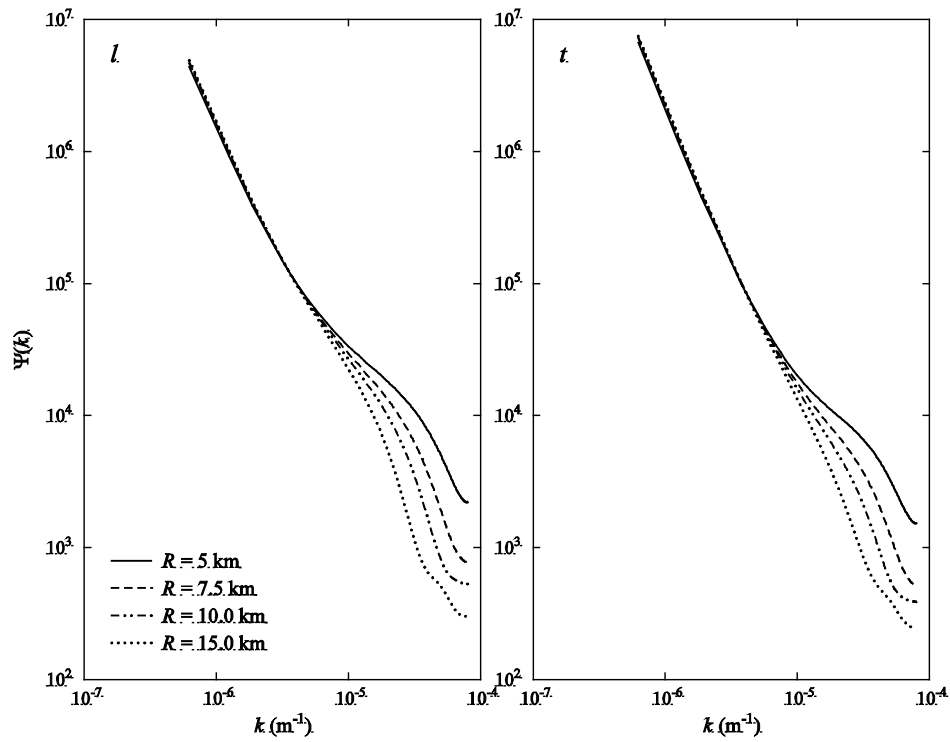
Figure 4.1 ASCAT-6.25 spectra with various values of the averaging radius for February 2 – 13, 2012.
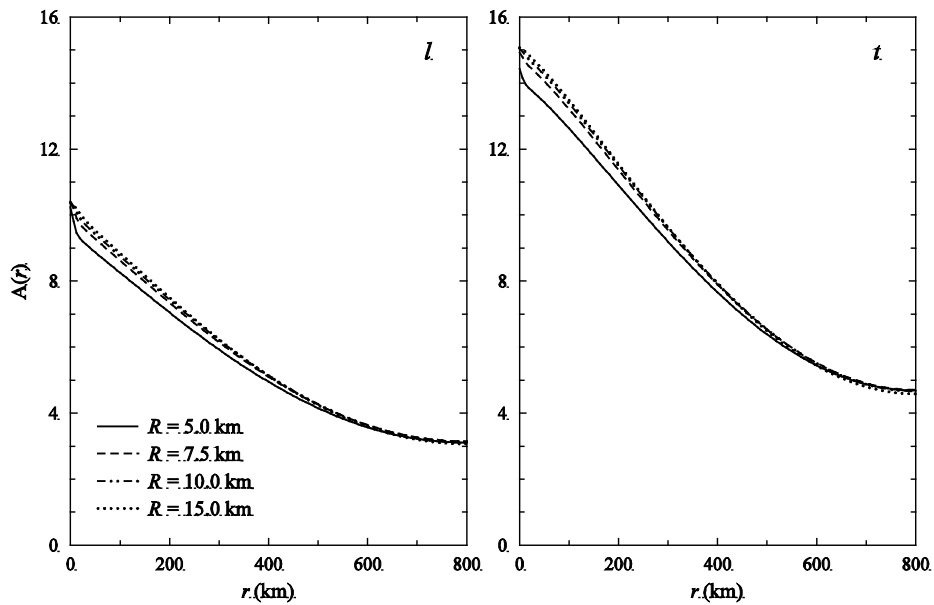
Figure 4.2 Autocovariance for ASCAT-6.25 with various values of the averaging radius for February 2 – 13, 2012.

4.3 Spatial variances

Figure 4.3 shows the spatial variance $V(r)$ (i.e., cumulative variance as function of scale r) and its derivative $dV(r)/dr$ (i.e., spatial variance density), both as a function of r, for the period February 2 – 13, 2012. The derivative of the spatial variance (lower panels) shows a significant peak at small distances with a maximum at the distance equal to the grid size. The peak lowers with increasing R and has almost disappeared for R equal to 15.0 km, the ASCAT-coastal value.

Figure 4.4 shows an enlargement of the $dV(r)/dr$ plot at small distances. Now each value is also indicated by a point, and the ASCAT-coastal results are also plotted in. Note that the ASCAT-coastal results indeed fall over those for R = 15.0 km.

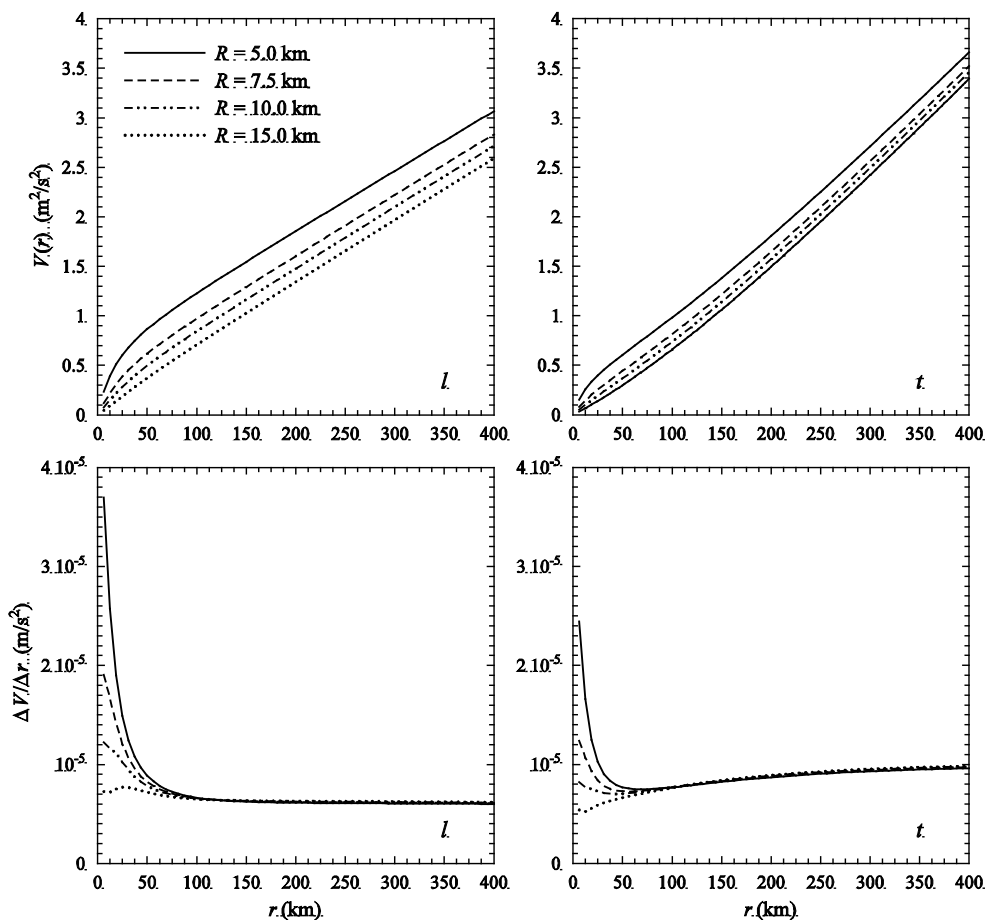**Figure 4.3** Spatial variance and its derivative for ASCAT-6.25 and ASCAT-coastal with various values of the averaging radius for February 2 – 13, 2012.
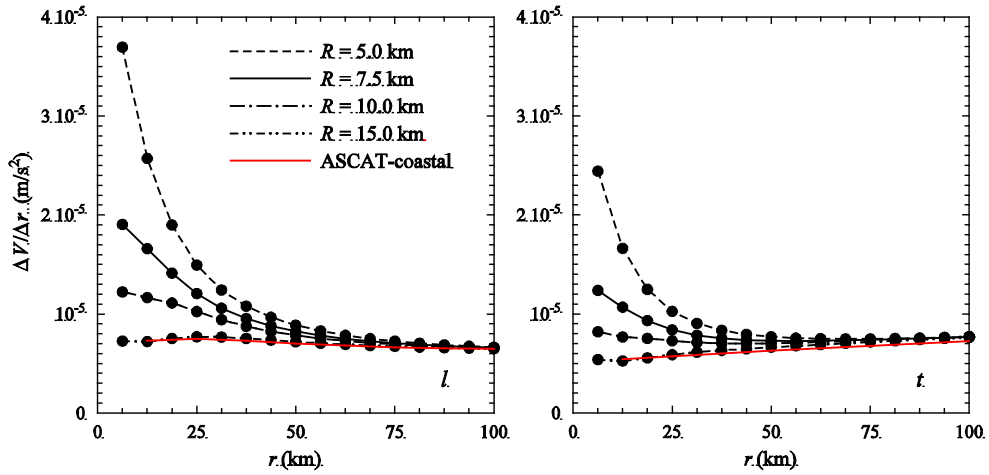
Figure 4.4 Enlargement of the spatial variance derivative at short distances for February 2 – 13, 2012.

From figures 4.3 and 4.4 one can infer that the ASCAT-6.25 products with R equal to 10.0 km, 7.5 km, and 5.0 km have an excess variance compared to the product with R = 15.0 km and the ASCAT-coastal product. The nature of this extra variance is not known a-priori: it may be noise caused by the smaller averaging area, but it may also be signal resolved with the finer footprints. The simulations in appendix F suggest that the origin is noise, as resolution improvement by averaging over a smaller area has a much less drastic effect.

Figure 4.3 suggests that for $r > 100$ km the spatial variance behaves like r^p with $p \approx 1$ for l and p slightly larger than 1 for l. This corresponds to a spectral power of -2 for l and a slightly smaller power (steeper spectrum) for t.

The value of the extra variance is simply the height above the R = 15.0 km curve at a lag of, say, r = 100 km in the upper panels of figure 4.3. Table 4.1 gives the values of these noise variances, denoted as ΔV_l and ΔV_t. Since the precise value of the spatial variance depends slightly on the sampling strategy adopted [*Vogelzang et al.,* 2015], table 4.1 gives the values for two sampling strategies:

1. **All points sampling**: all possible samples are taken into account with each sample weighted with the number of valid points it contains. Samples may be overlapping.
2. **Spectral sampling**: only non-overlapping samples without missing points are taken into account.

As can be inferred from table 4.1, the two sampling strategies give very similar values for the excess variance, except for ΔV_t at 5 km averaging radius. Therefore we will use the "All points sampling" strategy in the remainder of this chapter.

R (km)	ΔV_l (m²/s²)		ΔV_t (m²/s²)	
	All points	Spectral	All points	Spectral
5.0	0.52	0.48	0.32	0.21
7.5	0.26	0.25	0.16	0.15
10.0	0.14	0.13	0.08	0.07

Table 4.1 Excess variance w.r.t. the R = 15.0 km product at 100 km lag for February 2 – 13, 2012.

4.4   Error analysis

Spatial variance

In Appendix F it is shown how the excess covariance (variance and correlations) can be calculated from ΔV_l and ΔV_t. Table 4.2 gives the results for the longitudal wind component l of the February 2012 data as a function of n, the number of lags taken into account, based on the along-track spatial variances. For $n = 1$ only the variance σ^2 can be retrieved; for $n > 1$ also $n - 1$ correlations can be found. The excess variance in table 4.2 is that of the $R = 5.0$ km winds with respect to the $R = 15.0$ km winds.

n	σ^2	ρ_1	ρ_2	ρ_3	ρ_4	ρ_5	ρ_6
1	0.371	0.0	0.0	0.0	0.0	0.0	0.0
2	0.613	0.395	0.0	0.0	0.0	0.0	0.0
3	0.643	0.423	0.047	0.0	0.0	0.0	0.0
4	0.616	0.397	0.004	-0.044	0.0	0.0	0.0
5	0.591	0.372	-0.037	-0.088	-0.042	0.0	0.0
6	0.576	0.355	-0.066	-0.118	-0.070	-0.027	0.0
7	0.564	0.342	-0.087	-0.140	-0.092	-0.048	-0.020

Table 4.2 Along-track error analysis results as a function of n for February 2 – 13, 2012.

Table 4.2 shows that σ^2 peaks at a value of 0.643 m²/s² for $n = 3$, with correlation coefficients $\rho_1 = 0.423$ and $\rho_2 = 0.047$. For larger values of n the higher correlation coefficients become negative and increase with n, while σ^2 and ρ_1 decrease. The same behaviour is found for t and for the August 2013 data at all values of R. Therefore $n = 3$ seems to be the best choice.

Tables 4.3 and 4.4 show both along-track and cross-track error analysis results for the periods February 2012 and August 2013, respectively, as a function of R, taking $R = 15.0$ km as reference dataset. The results in tables 4.3 and 4.4 are very similar. The variance decreases with increasing averaging radius R, while the correlation coefficients increase. The latter effect is explained in chapter 6 as being caused by increase of the overlap in spatial response

between adjacent WVC's (in the azimuth direction) with increasing averaging radius. Note that the numerical values are close to each other for the two periods.

type	R (km)	Longitudal component l			Transversal component t		
		σ^2 (m^2/s^2)	ρ_1	ρ_2	σ^2 (m^2/s^2)	ρ_1	ρ_2
along track	5.0	0.643	0.423	0.047	0.394	0.396	0.036
	7.5	0.344	0.572	0.127	0.198	0.560	0.116
	10.0	0.182	0.659	0.230	0.100	0.651	0.230
cross track	5.0	0.560	0.228	0.004	0.384	0.250	0.014
	7.5	0.283	0.473	0.056	0.193	0.492	0.068
	10.0	0.147	0.604	0.227	0.101	0.620	0.240

Table 4.3 Error analysis results February 2 – 13, 2012.

type	R (km)	Longitudal component l			Transversal component t		
		σ^2 (m^2/s^2)	ρ_1	ρ_2	σ^2 (m^2/s^2)	ρ_1	ρ_2
along track	5.0	0.598	0.420	0.045	0.388	0.400	0.037
	7.5	0.326	0.569	0.125	0.195	0.558	0.114
	10.0	0.173	0.656	0.227	0.098	0.647	0.226
cross track	5.0	0.517	0.228	0.009	0.383	0.257	0.018
	7.5	0.264	0.473	0.062	0.193	0.493	0.069
	10.0	0.138	0.603	0.229	0.100	0.619	0.238

Table 4.4 Error analysis results August 2013.

Buoy comparison

Another way to get more information on the ASCAT-6.25 products is to compare them with buoy measurements. The results are shown in tables 4.4 and 4.5 for the periods February 2012 and August 2013, respectively. Results are shown for ASCAT-6.25 products with R = 5.0, 7.5, 10.0, and 15.0 km. Only collocations that are common to all five products are considered.

Tables 4.5 and 4.6 give the standard deviations of the differences in buoy wind and scatterometer wind for speed, direction, components u and v, and components l and t. The last row of each table gives an estimate of the accuracy. The number of collocations in tables 4.5 and 4.6 is 942 and 2682, respectively, except for the comparison in direction, where a threshold wind speed of 4 m/s was applied because at lower wind speeds the direction is not well defined.

Table 4.5 shows that the differences in u and t decrease with increasing value of R, while those in v and l show an increasing trend, though not as regular. Nevertheless, the dataset is very small, only 942 points, so the statistical accuracy is about 3.3%. As a consequence, the differences in table 4.5 are statistically not significant.

R (km)	σ_s (m/s)	σ_{dir} (deg)	σ_u (m/s)	σ_v (m/s)	σ_l (m/s)	σ_t (m/s)	N
5.0	1.05	19.8	1.76	1.98	1.99	1.75	942
7.5	1.01	20.2	1.73	1.95	1.96	1.71	942
10.0	1.01	20.8	1.70	2.02	2.04	1.68	942
15.0	1.00	20.5	1.67	2.02	2.03	1.66	942
precision	0.03	0.7	0.06	0.07	0.07	0.06	

Table 4.5 Buoy comparison for February 2 – 13, 2012.

R (km)	σ_s (m/s)	σ_{dir} (deg)	σ_u (m/s)	σ_v (m/s)	σ_l (m/s)	σ_t (m/s)	N
5.0	1.01	17.9	1.41	1.70	1.70	1.42	2682
7.5	0.99	16.6	1.38	1.64	1.64	1.39	2682
10.0	0.98	16.9	1.37	1.62	1.61	1.37	2682
15.0	0.98	16.8	1.36	1.59	1.59	1.36	2682
precision	0.02	0.3	0.03	0.03	0.03	0.03	

Table 4.6 Buoy comparison for August 2013.

Table 4.6 is based on 2682 collocations, resulting in a slightly better statistical accuracy of 2%. All differences increase with decreasing R, but as before the differences are hardly significant, except the extreme differences for l and t. Note that the scatterometer winds compare better with buoys for August 2013 than for February 2012, in particular for the wind direction and the wind components.

Triple collocation

Finally, tables 4.7 and 4.8 show the triple collocation results as a function of averaging radius R for the periods February 2012 and August 2013, respectively. The tables show the error standard deviations for l and t, σ_l and σ_t, the number of collocations used to arrive at the error estimates, N, and the representativeness error variances obtained from the spatial variances at a scale of 200 km, r_l^2 and r_t^2. The triple collocation analysis started with collocations common to all values of R. The last row gives the accuracy of the errors estimated under the assumption that the errors are Gaussian.

	buoys		scatterometer		background		N	r_l^2 (m^2/s^2)	r_t^2 (m^2/s^2)
R (km)	σ_l (m/s)	σ_t (m/s)	σ_l (m/s)	σ_t (m/s)	σ_l (m/s)	σ_t (m/s)			
5.0	1.23	1.28	1.15	0.84	1.61	1.53	930	0.85	1.17
7.5	1.26	1.28	1.06	0.78	1.58	1.54	930	0.66	0.91
10.0	1.25	1.26	0.96	0.75	1.60	1.55	929	0.56	0.76
15.0	1.29	1.29	0.89	0.73	1.56	1.58	931	0.46	0.63
precision	0.13	0.15	0.12	0.10	0.11	0.10			

Table 4.7 Triple collocation results for February 2012.

	buoys		scatterometer		background		N	r_l^2 (m^2/s^2)	r_t^2 (m^2/s^2)
R (km)	σ_l (m/s)	σ_t (m/s)	σ_l (m/s)	σ_t (m/s)	σ_l (m/s)	σ_t (m/s)			
5.0	0.97	1.02	1.23	0.80	1.40	1.24	2655	1.10	1.37
7.5	1.00	1.02	1.11	0.74	1.39	1.22	2653	0.87	1.11
10.0	1.02	1.03	1.08	0.68	1.39	1.24	2655	0.75	0.97
15.0	1.01	1.04	1.02	0.65	1.40	1.21	2652	0.64	0.83
precision	0.08	0.08	0.08	0.06	0.05	0.03			

Table 4.8 Triple collocation results for August 2013.

The results in tables 4.7 and 4.8 are remarkably consistent, despite the small number of collocations. The buoy errors and the background errors are independent of the averaging radius within the estimated precision, while the scatterometer errors increase with decreasing R, though the increase is only significant between $R = 15$ km and $R = 5$ km. The buoy errors are the same for l and t, whereas the scatterometer and background errors are larger for l than for t. Finally, the buoy and background errors are larger for February 2012 than for August 2013, while the scatterometer errors are about the same and the representativeness errors are smaller.

Discussion

The spatial variance error analysis shows a considerable increase in noise w.r.t. the ASCAT coastal product when going to a smaller averaging radius. This is confirmed by the triple collocation analysis, but only significant between $R = 15$ km and $R = 5$ km. It is not found back in the buoy comparisons – there no significant effect is found. Table 4.9 shows the standard deviation of the difference between scatterometer and buoy winds calculated directly (from tables 4.5 and 4.6, labelled direct) and from the triple collocation results in tables 4.7 and 4.8 (labelled TC). As can be seen from table 4.9 the standard deviations in the wind velocity differences calculated from the triple collocation results are rather imprecise, because

the errors add. Within the estimated precision, also the triple collocation estimates show no significant effect.

R (km)	February 2012				August 2013			
	σ_l (m/s)		σ_t (m/s)		σ_l (m/s)		σ_t (m/s)	
	direct	TC	direct	TC	direct	TC	direct	TC
5.0	1.99	1.68	1.75	1.53	1.70	1.57	1.42	1.30
7.5	1.96	1.65	1.71	1.50	1.64	1.49	1.39	1.26
10.0	2.04	1.57	1.68	1.47	1.61	1.49	1.37	1.23
15.0	2.03	1.54	1.66	1.48	1.59	1.44	1.36	1.23
precision	0.07	0.17	0.06	0.18	0.03	0.11	0.03	0.10

Table 4.9 Standard deviation of wind speed difference between scatterometer and buoys calculated directly (direct) and obtained from triple collocation results (TC).

Note that the direct differences in table 4.9 are larger than those obtained from triple collocation. This is because during triple collocation some outliers are removed, reflected in the different values of N between tables 4.5 and 4.7 and tables 4.6 and 4.8.

The spatial variance analysis assumes that the signal content of the various wind products is independent of the averaging radius. When going to smaller averaging radius, one expects the effective resolution to improve and thus the signal content at small distances to increase. Therefore the spatial variance analysis may overestimate the errors because its reference level is too low, though the simulations in appendix F suggest that this effect is small.

R (km)	February 2012				August 2013			
	$\Delta\sigma_l^2$ (m^2/s^2)		$\Delta\sigma_t^2$ (m^2/s^2)		$\Delta\sigma_l^2$ (m^2/s^2)		$\Delta\sigma_t^2$ (m^2/s^2)	
	TC	SV	TC	SV	TC	SV	TC	SV
5.0	0.56	0.64	0.20	0.39	0.52	0.60	0.25	0.39
7.5	0.31	0.34	0.09	0.20	0.21	0.33	0.14	0.30
10.0	0.13	0.18	0.04	0.10	0.10	0.17	0.06	0.10

Table 4.10 Excess variances w.r.t. 15 km averaging radius from triple collocation (TC) and spatial variance analysis (SV).

Table 4.10 gives the excess variances calculated from the triple collocation results (by taking the values for $R = 15$ km as reference, labelled TC) and from the spatial variance analysis (from tables 4.3 and 4.4, labelled SV). As can be seen from table 4.9 the spatial variance analysis indeed yields slightly higher values for the excess variance than the triple collocation analysis, but the difference is small and hardly significant because of the limited accuracy of

the triple collocation results. Moreover, the spatial variance analysis covers all Earth while the triple collocation analysis is restricted to the buoy locations.

This leads to the conclusion that the ASCAT-6.25 wind products with an averaging radius smaller than 15 km contain more noise, as identified by the spatial variance analysis and, to some extend, by the triple collocation analyses. The fact that the buoy errors from the triple collocation analysis remain constant indicates that the ASCAT-6.25 km products with $R = 7.5$ km or $R = 5$ km do not contain much additional detail compared to the product with $R = 15$ km. However, the dataset is too small to arrive at definitive conclusions, and the analysis should be repeated for one or more years of data.

4.5   Dependency on WVC number

Figure 4.5 shows the spatial variance and its derivative of the ASCAT-6.25 km product with averaging radius R = 15 km, the value used for the ASCAT-coastal product, for various values for the WVC number in the left swath, ranging from WVC=1 (largest incidence angle) to WVC 81 (second smallest incidence angle). The figure shows that the noise peak is effectively suppressed, though some traces of it can be seen at small distances. The figure also shows that the spatial variances clearly depend on WVC number.

The derivative of the spatial variance in the along-track velocity component l increases with increasing WVC number, as the lower left panel of figure 4.5 shows, except for WVC 81. Equivalently, the slope of the spatial variance in l increases with decreasing incidence angle, except for the smallest incidence angles. The results for the spatial variance in the cross-track wind component t show less dependency on WVC number, except for WVC 81.
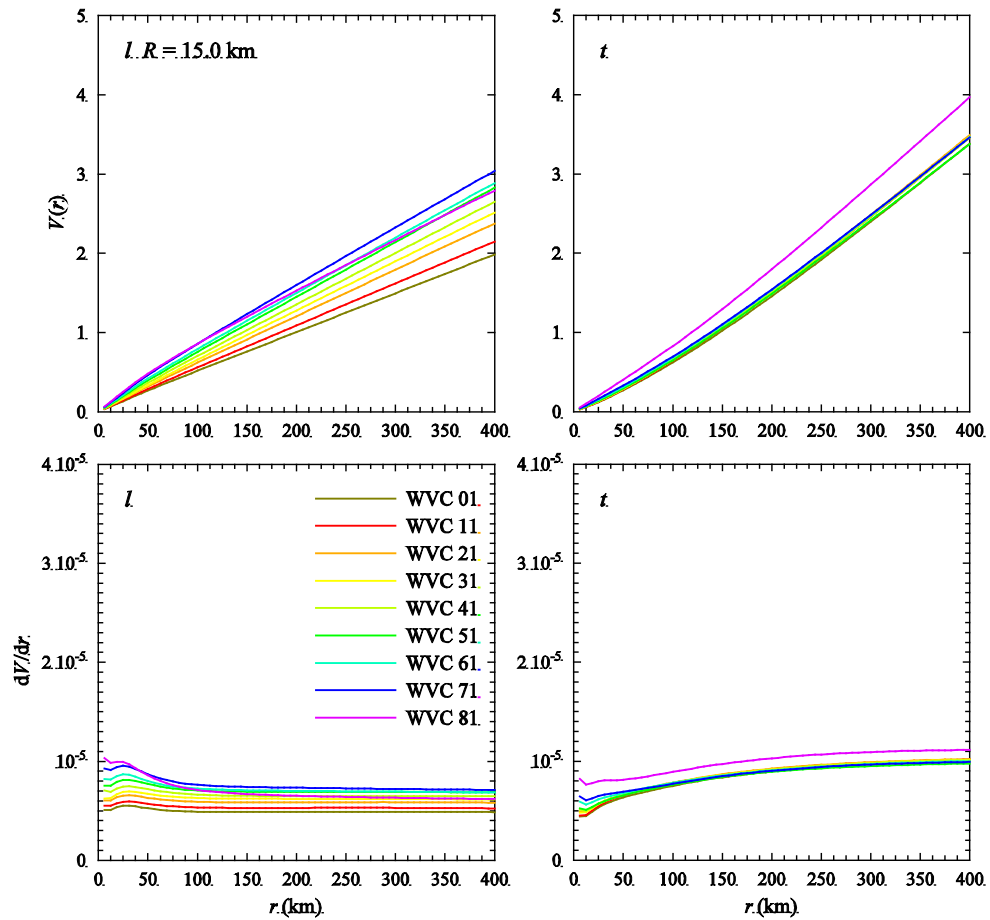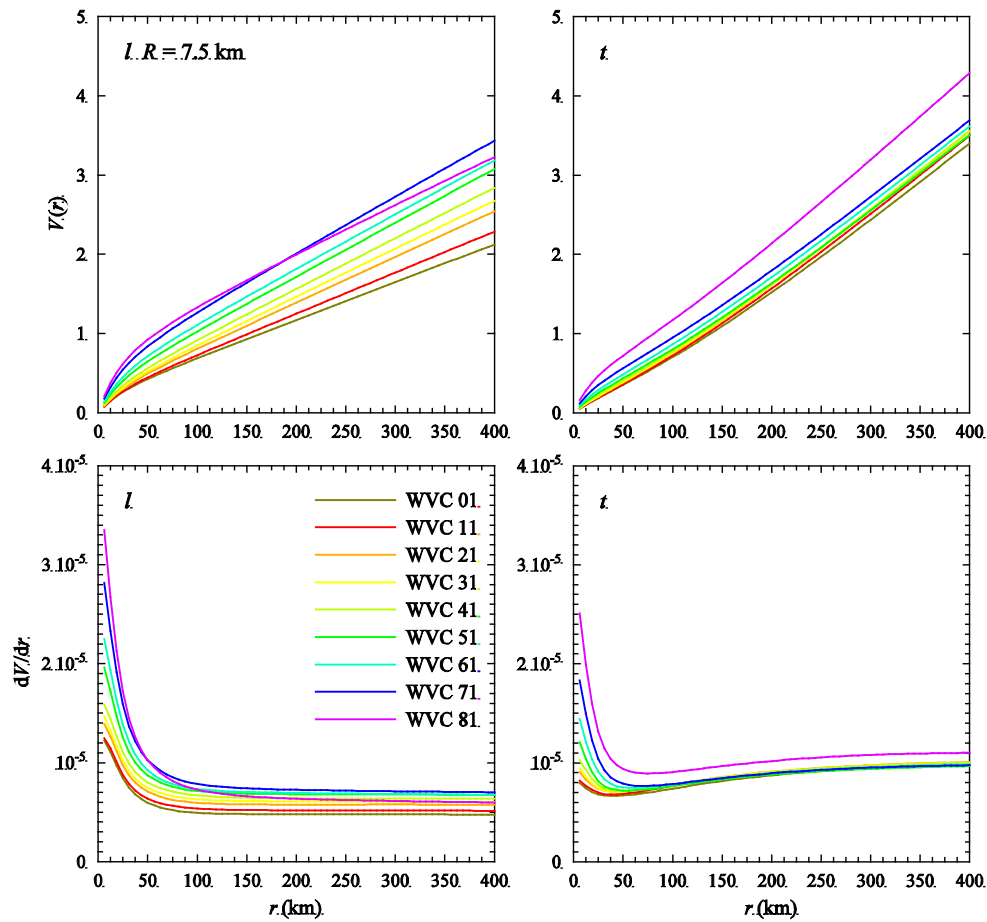
Figure 4.5 Spatial variance and its derivative for ASCAT-6.25 with $R = 15.0$ km for various values of the WVC number for February 2 – 13, 2012.

Figure 4.6 is similar to figure 4.5, except that the averaging radius R equals 7.5 km. The noise peaks are clearly visible, as in figure 4.3. The figure shows that the noise peak is highest for small incidence angles and lowest for high incidence angles. Note that the spatial variances for t, upper right panels of figures 4.5 and 4.6, show more spreading for $R = 7.5$ km than for $R = 15.0$ km.

Figure 4.6   Spatial variance and its derivative for ASCAT-6.25 with $R = 7.5$ km for various values of the WVC number for February 2 – 13, 2012 .

Figures 4.5 and 4.6 suggest a sudden change in the structure function behavior at small incidence angles. However, as shown in figure 4.7, this is not the case: the spatial variances change quite smoothly with WVC number at small incidence angle, though the changes are larger than at high incidence angles.

A final point to note is that the height of the noise peaks in figures 4.3 and 4.4 decreases with increasing averaging radius R, but that their width is independent of R. The same applies for the WVC dependency in figures 4.5-4.7: the height of the noise peak varies but its width remains the same. This must be due to the footprint size of the basic radar cross sections used for aggregation within WVC's.
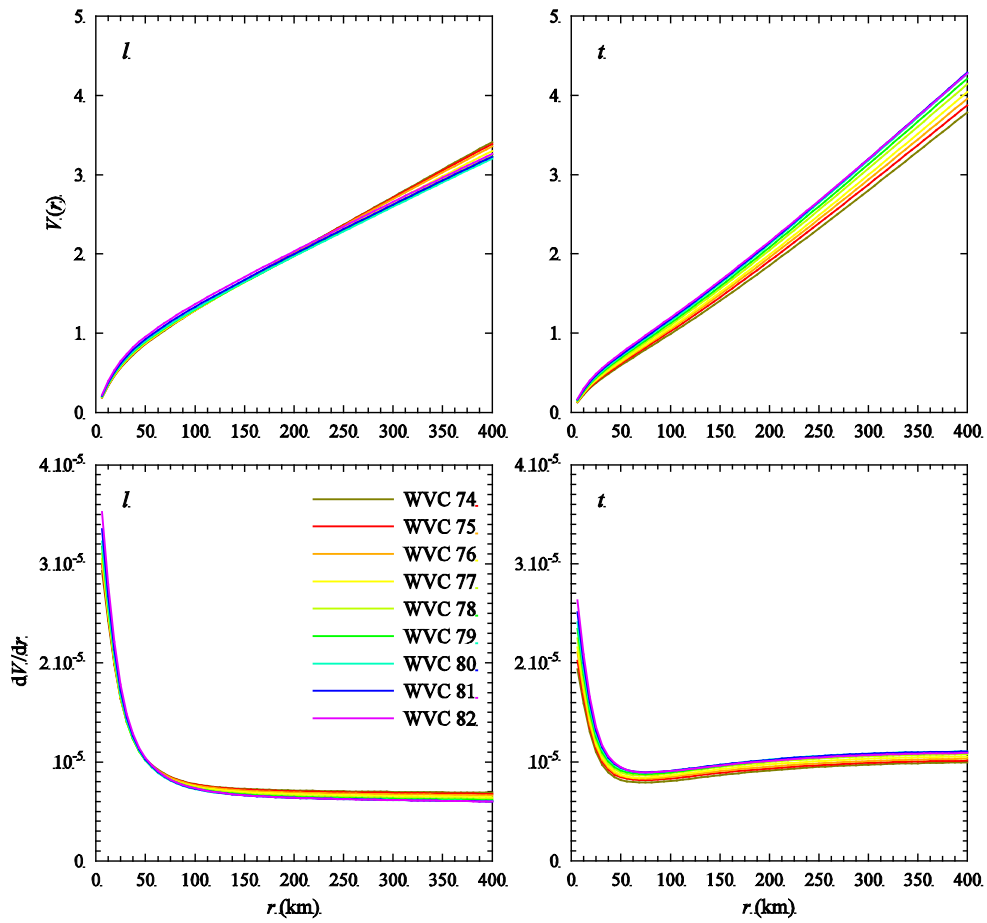
Figure 4.7 Spatial variance and its derivative for ASCAT-6.25 with R = 7.5 km for WVC 74 to 82 for February 2 – 13, 2012 .

5 ASCAT spatial response

5.1 Footprints

Figure 5.1 shows the centers of the full resolution footprints contributing to ASCAT-coastal WVC 42 (left hand panels), WVC 62 (mid panels), and WVC 82 (right hand panels) as red crosses. The WVC's are on the right hand swath of ASCAT at low, medium, and high incidence angle, respectively. Results are shown for the fore beam (upper panels), mid beam (middle panels), and aft beam (lower panels). The solid box shows the WVC with sides 12.5 by 12.5 km. The dotted circle shows the averaging region with a radius R equal to 15 km. The WVC's were chosen along the equator, so the latitude-longitude plots in figure 5.1 indicate the true geometry.
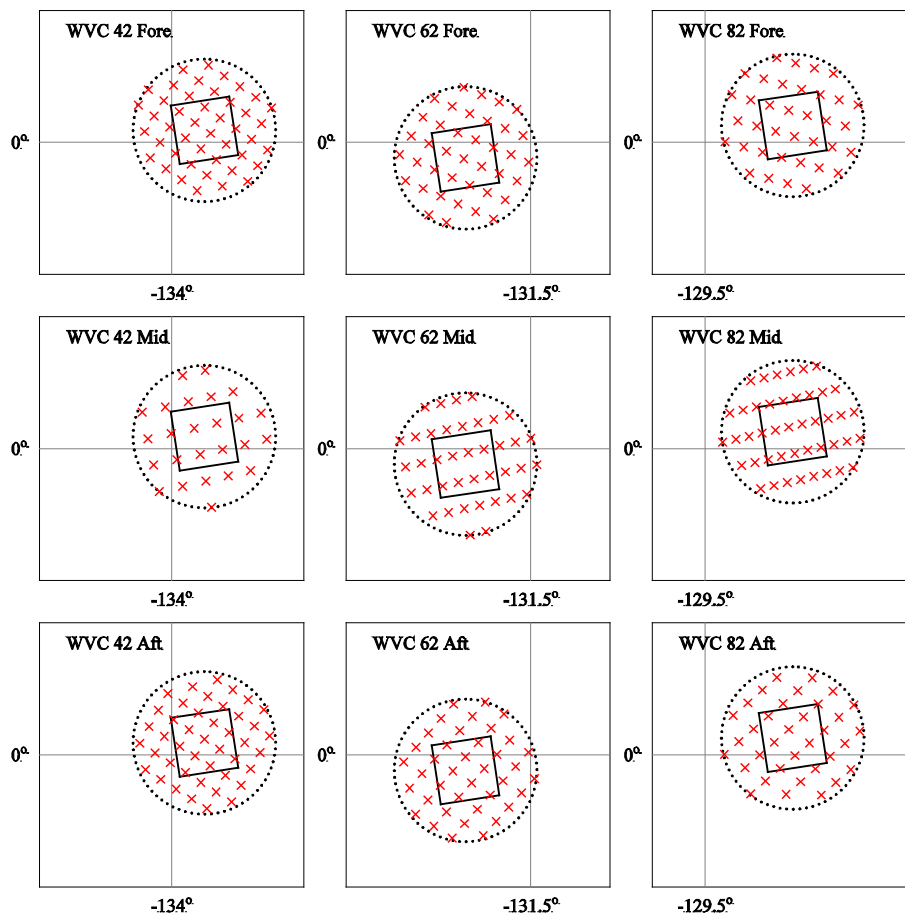
Figure 5.1 Distribution of the full resolution footprints.

Figure 5.1 shows that the density of full resolution footprints for the mid beam increases with incidence angle. Notably at very low incidence angles the number of full resolution footprints contributing to the cross section of a WVC is rather small. For the fore and aft beams the situation is reverse: here the density of contributing full resolution footprints decreases with increasing incidence angle, though not as strongly.

Note that the edges of the WVC are not parallel to the mid-beam azimuth and range directions as indicated by the crosses. This is because at the moment the mid beam hits a WVC on the equator, the satellite is still south of the equator. Therefore the WVC orientation differs slightly from the beam orientation.

The results in figure 5.1 are confirmed by figure 5.2, which shows the maximum number of full resolution footprints contribution to a WVC as a function of WVC number for the fore, mid, and aft beams. Figure 5.2 is for ASCAT-coastal, and shows that the number of full resolution footprints contributing to a WVC for the mid beam decreases from about 50 at high incidence angles to about 30 at low incidence angles. For the fore and aft beams this relation is reversed and the variation in the number of contributing footprints is smaller.
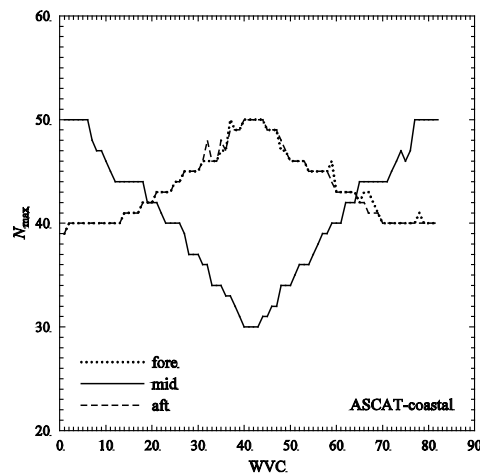

Figure 5.2   Maximum number of contributing footprints as a function of WVC number.

Finally, figure 5.3 shows the maximum number of contributing full resolution footprints as a function of geographical latitude for WVC's 1, 21, and 41 (left hand swath) and WVC's 42,62, and 82 (right hand swath. Figure 5.3 shows that the maximum number of contributing footprints varies slightly with latitude, due to the non-spherical shape of the Earth, and that the affect is symmetrical with respect to the equator for the left and right swath.
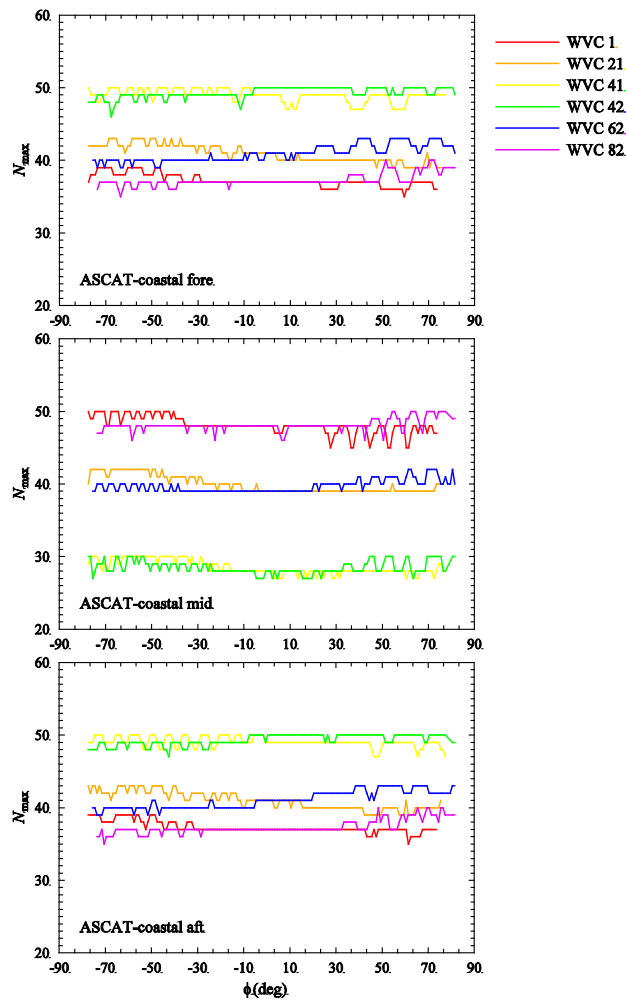
Figure 5.3   Maximum number of contributing footprints as a function of latitude.

5.2   *Spatial Response Functions*

Richard Lindsley and Dave Long kindly provided us with their code for calculating the ASCAT spatial response function (SRF) [*Lindsley,* 2014; *Lindsley et al*., 2015]. Figure 5.4 shows the SRF for a single full resolution footprint, normalized to a maximum value of 1, plotted over the same WVC geometry as figure 5.1.

Figure 5.4 shows that the spatial response is not aligned in the range or azimuth direction, because of the Doppler effect that causes the pattern to rotate. Without this effect the spatial response is much larger in the along-track (azimuth) direction than in the cross-track (range) direction, in particular for the mid beam at high incidence angles, but that the pattern is

rotated. Following the 3dB contour (SRF value about 0.5) given by the green region, the size of a single full resolution footprint is of the order of 30 km in azimuth and 10 km or less range.
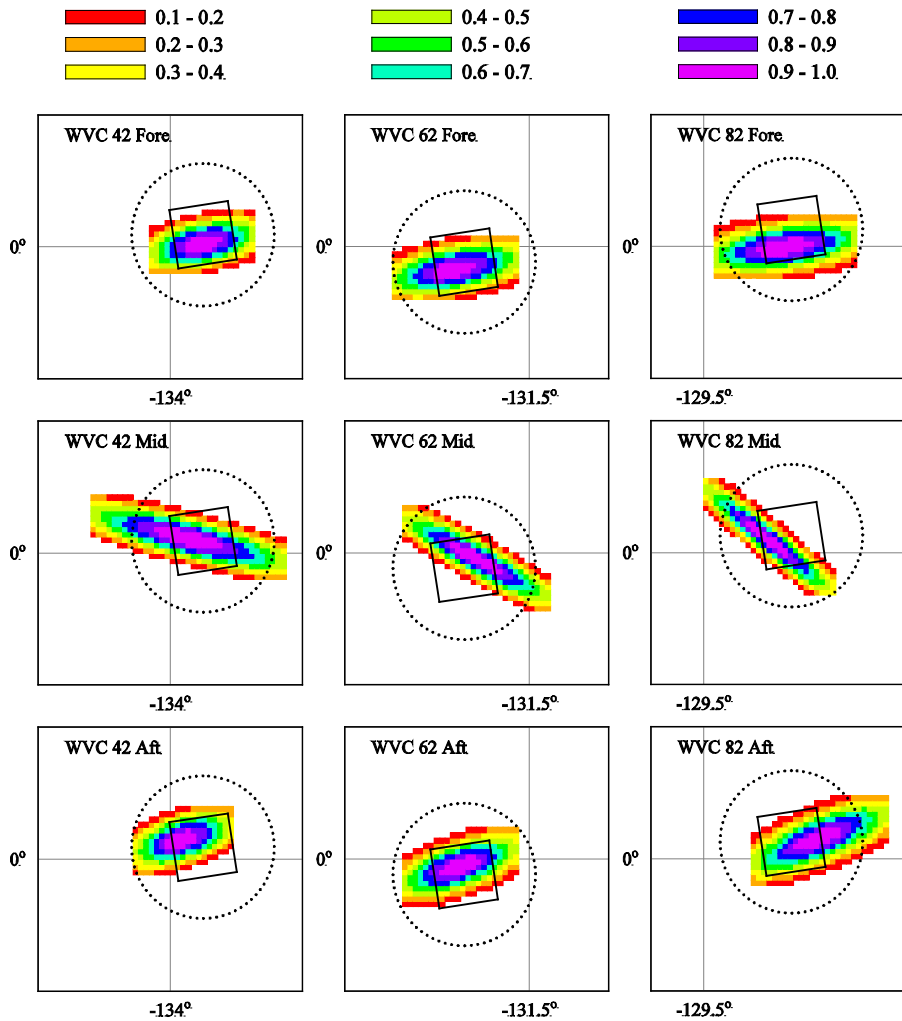
Figure 5.4 Spatial response functions for a single full resolution footprint.

Figure 5.5 shows the cumulative SRF (i.e., the sum of all SRF's contributing to a WVC renormalized to 1) for ASCAT-coastal. The most circular cumulative SRF (CSRF) is found for the fore and aft beam, while for the mid beam the response is more irregular, due to the elongated shape of the footprints there. Note that the 3dB countour (extent of the green region) follows quite well the dotted circle that indicates the extent of the averaging area (radius 15 km).
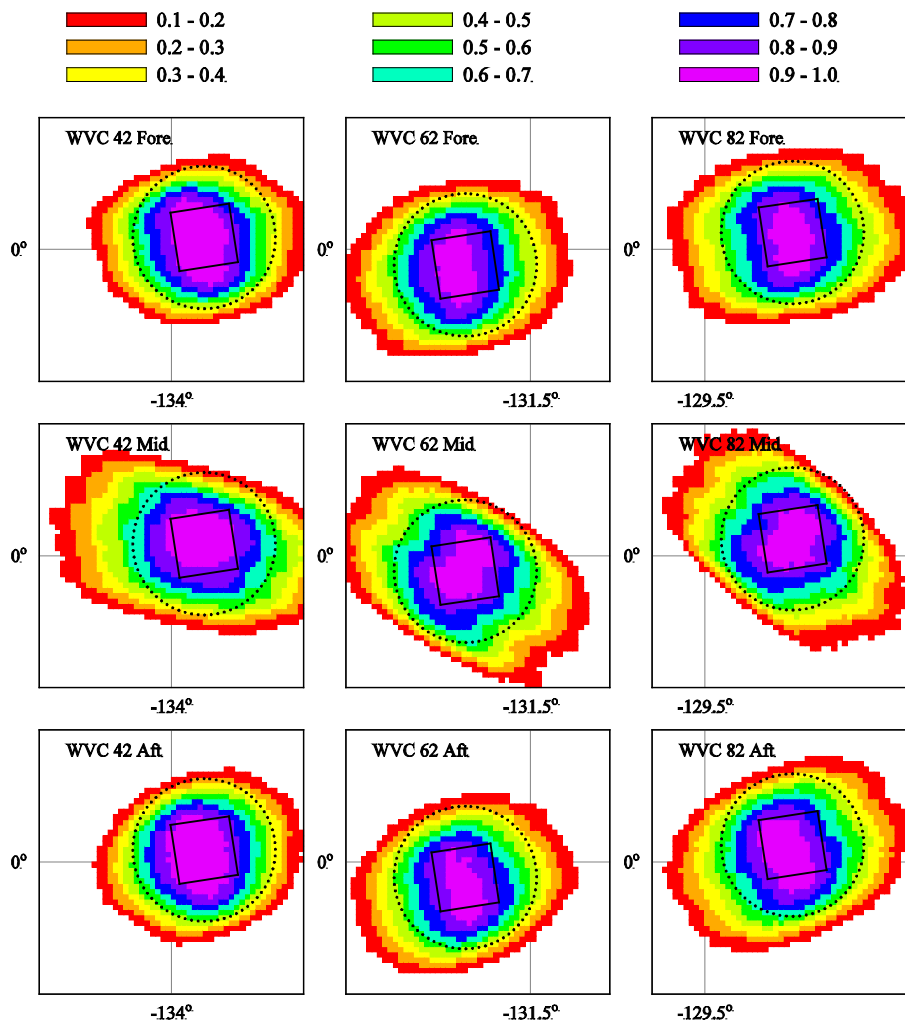
Figure 5.5 Cumulative spatial response functions for a ASCAT-coastal.

Figure 5.6 is similar to figure 5.5, but now for ASCAT-6.25 with an averaging radius of 7.5 km. The 3dB contour now has a more elliptical shape, in particular for the mid beam, and frequently falls outside the averaging region indicated by the dotted circle with radius 7.5 km.
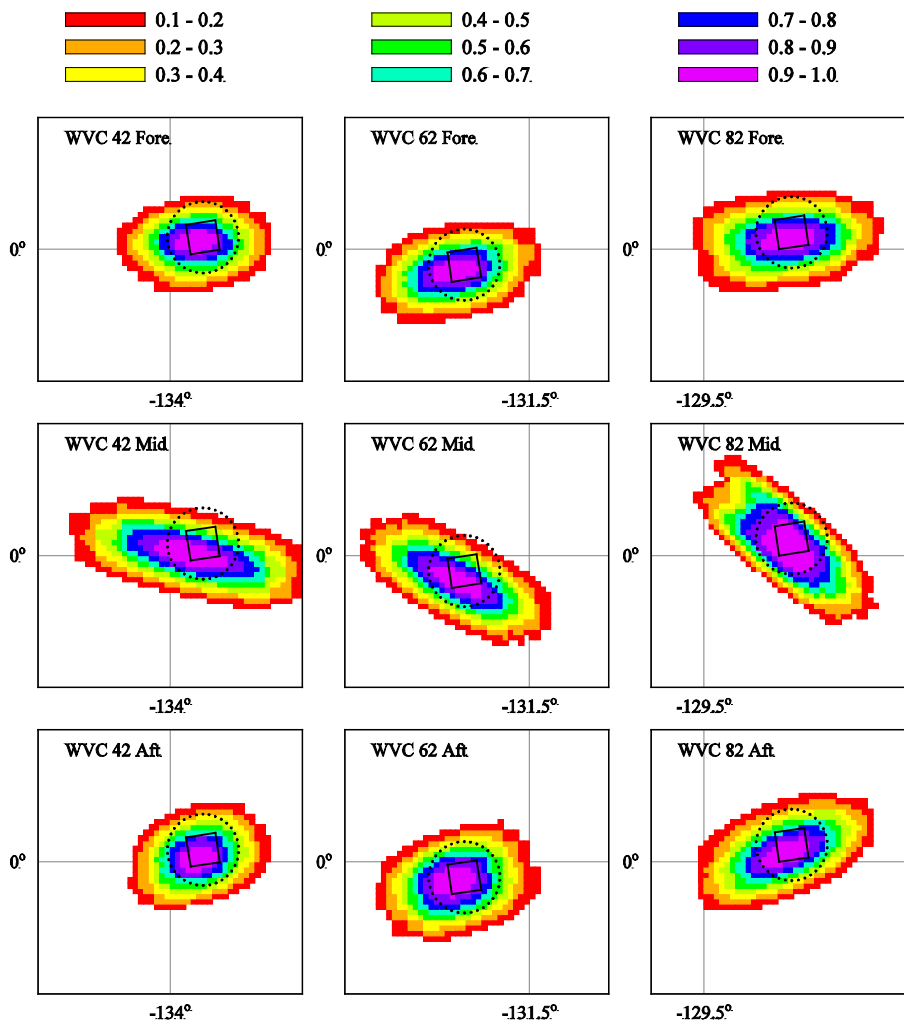
Figure 5.6 Cumulative spatial response functions for a ASCAT-6.25.

5.3 Simulated single target

The spatial response function software can also be used to simulate a single bright target of unit strength against a dark background. When the position of the target is given, for instance as the centre of the WVC's in figure 5.1, and the spatial response function is constructed for each of the full resolution footprints in figure 5.1, then the value of the spatial response function for each footprint evaluated for the WVBC centre is a measure for the brightness of the full resolution cell caused by the target, provided the spatial response functions are properly normalized to 1. Figure 5.7 shows the results of this exercise.
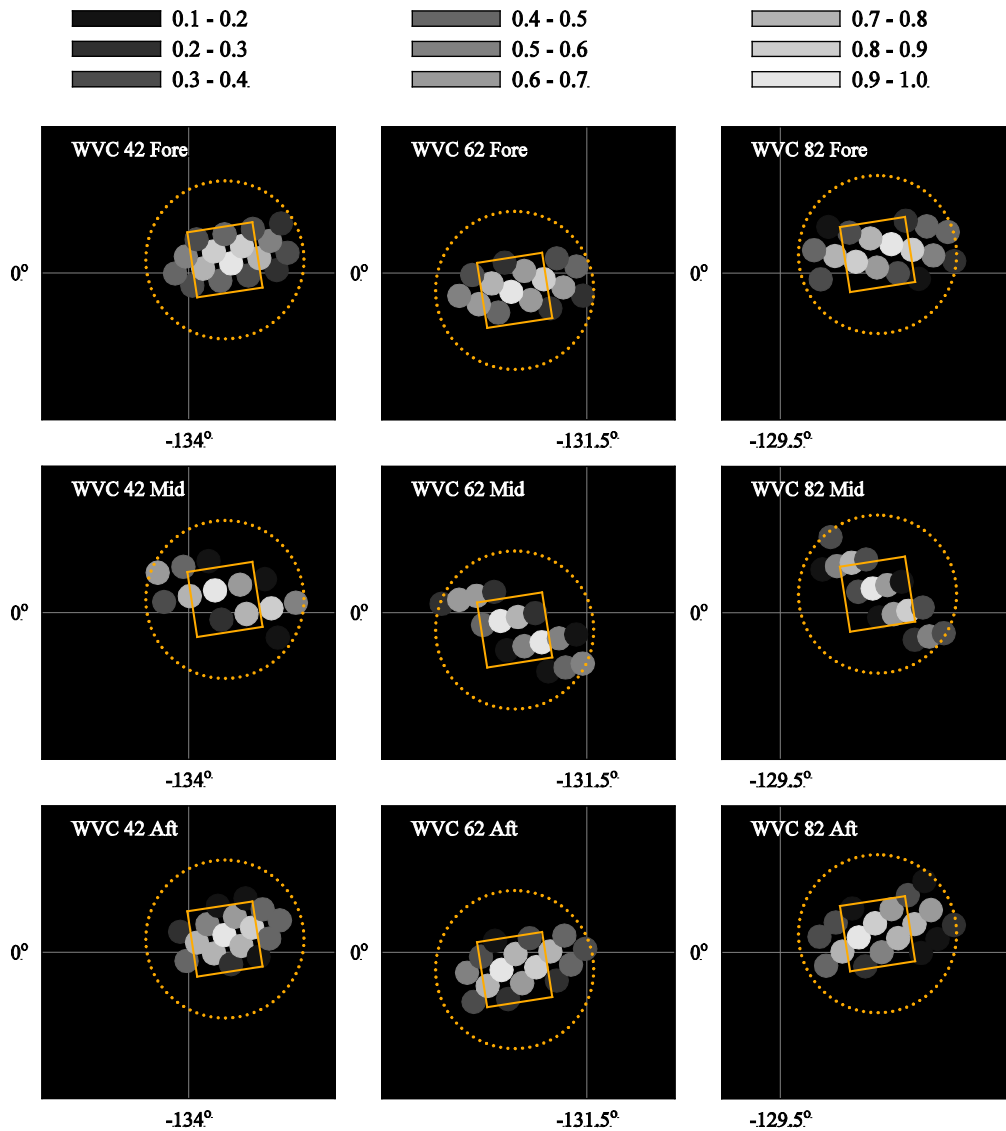
Figure 5.7 Simulated full resolution images for a single target at the WVC origin.

Figure 5.7 shows (parts of) simulated full resolution images for a single target at the WVC centre. Each full resolution pixel is given by a circle. The figure shows that a single bright target is smeared out in the full resolution image over 5-7 pixels in azimuth and 3-4 pixels in range, in agreement with observations. Note that the 15 km averaging radius (orange dotted circles) encloses the single target image in the full resolution image, another indication that this value is well chosen. The size of the image of a single target is comparable to or even greater than a 12.5 km WVC (orange square), notably in the azimuth direction.

6 Aggregation optimalisation

6.1 Introduction

For the mid beam, the ASCAT-coastal and ASCAT-6.25 cumulative spatial response functions (CSRF's) shown in figures 6.5 and 6.6, respectively, clearly has an elongated shape in the direction of the individual footprints or spatial response functions (SRF's) shown in figure 5.4. The CRSF's for the fore and aft beam are much more circular. This causes sampling differences between the mid beam and the fore and aft beams. These differences may be reduced by adapting the aggregation area for the mid beam such that the mid beam CSRF more resembles the fore and aft beam CSRF's.

In section 6.2 an elliptical aggregation area for the mid beam will be investigated. It will be shown that this does not help much, because the number of SRF's contributing to the CSRF reduces, causing more noise in the CSRF. This is in particular the case at low incidence angles, where the spreading between the mid beam SRF's is large (see figure 5.1). Moreover, the location of the center of the aggregation area may be such that the spatial pattern of the contributing SRF's is asymmetric, causing asymmetric CRSF's.

The latter point is further investigated in section 6.3. Here the center of the aggregation area is shifted to a more symmetric position with respect to the SRF centers. This has a beneficial effect for some choices (but not for all choices), except at low incidence angles. This is caused by the fact that the spatial distribution of the SRF centers is not uniform here: the density rapidly increases with incidence angle. The underlying reason is, of course, that the SRF centers are uniform in range, but their ground projection is not, the strongest effect being at small incidence angles.

The results in this chapter are for ASCAT-coastal only.

6.2 Elliptical aggregation area

Suppose we have two points, with longitudes and latitudes (λ_1, φ_1) and (λ_2, φ_2), respectively. Suppose point 1 is the center of a WVC and point 2 the center of a SRF. For the default circular aggregation area in AWDP the SRF contributes to the WVC if its center is within the aggregation area, i.e.,

$$d = 2\pi R_e \frac{\Delta \sigma}{360} < r \quad , \tag{6.1}$$

where r is the radius of the aggregation area (15 km for ASCAT-coastal), R_e the radius of the Earth, and $\Delta\sigma$ the angular distance between the two points. The exact expression for $\Delta\sigma$ reads [*Williams*, 2011]

$$\Delta\sigma = \arcsin\left(\sqrt{\sin^2\left(\tfrac{1}{2}\Delta\varphi\right) + \cos\varphi_1 \cos\varphi_2 \sin^2\left(\tfrac{1}{2}\Delta\lambda\right)}\right) \quad , \tag{6.2}$$

with $\Delta\varphi = \varphi_1 - \varphi_2$ and $\Delta\lambda = \lambda_1 - \lambda_2$. For small distances we this reduces to

$$\Delta\sigma = \sqrt{(\Delta\varphi)^2 + \cos^2\varphi(\Delta\lambda)^2} \quad , \tag{6.3}$$

using $\cos\varphi_1 \approx \cos\varphi_2 = \cos\varphi$. This is the equation implemented in AWDP. Note that this is the distance obtained from the Pythagorean theorem with $\Delta\varphi$ the North-South distance and $\cos\varphi(\Delta\lambda)$ the East-West distance.

For an elliptical aggregation area we introduce local flat coordinates (ξ,η) with ξ parallel to the long axis of the SRF and η perpendicular to it (see figure 6.4). The angle γ between the ξ-axis and the East is given by

$$\gamma = \alpha + \beta + \tfrac{1}{2}\pi \quad , \tag{6.4}$$

with α the angle between the WVC range direction and the East, and β the angle between the range direction and the SRF orientation. The term $\tfrac{1}{2}\pi$ must be included because the long axis of the aggregation area is perpendicular to that of the SRF. The angle β has been obtained manually from figure 6.4 for the mid beam. It equals -23° for WVC 42, -40° for WVC 62, and -50° for WVC 82

Now a SRF contributes a WVC if

$$f^2\xi^2 + \eta^2 < r^2 \quad , \tag{6.5}$$

with

$$\begin{aligned} \xi &= \Delta x \cos\gamma + \Delta y \sin\gamma \\ \eta &= -\Delta x \sin\gamma + \Delta y \cos\gamma \end{aligned} \quad . \tag{6.6}$$

where

$$\Delta x = R_e \cos\left(\frac{\varphi_1 + \varphi_2}{2}\right)\Delta\lambda \quad , \quad \Delta y = R_e \Delta\varphi \quad . \tag{6.7}$$

The effect of increasing f^2 is to narrow the aggregation area in the direction of the SRF's.
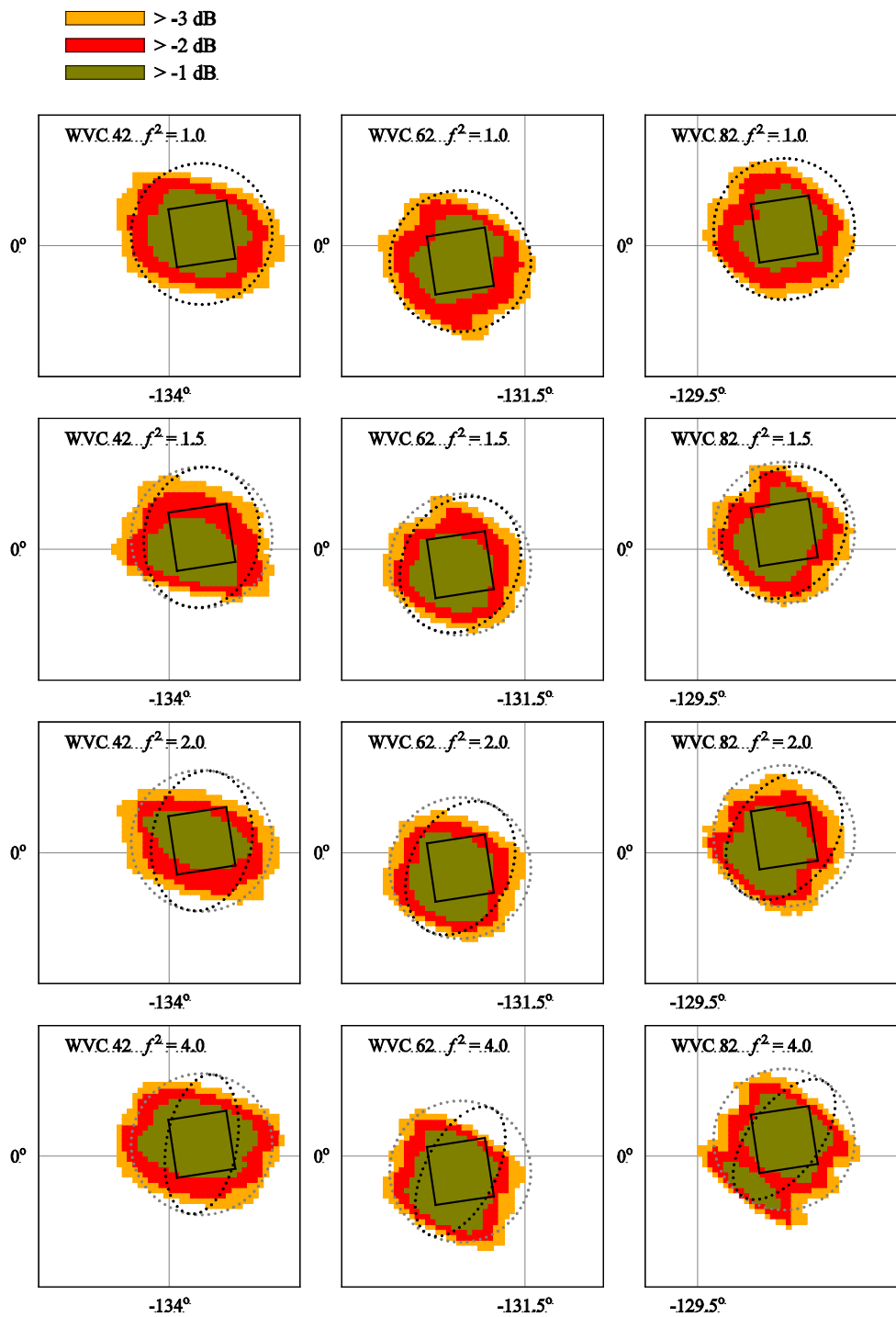
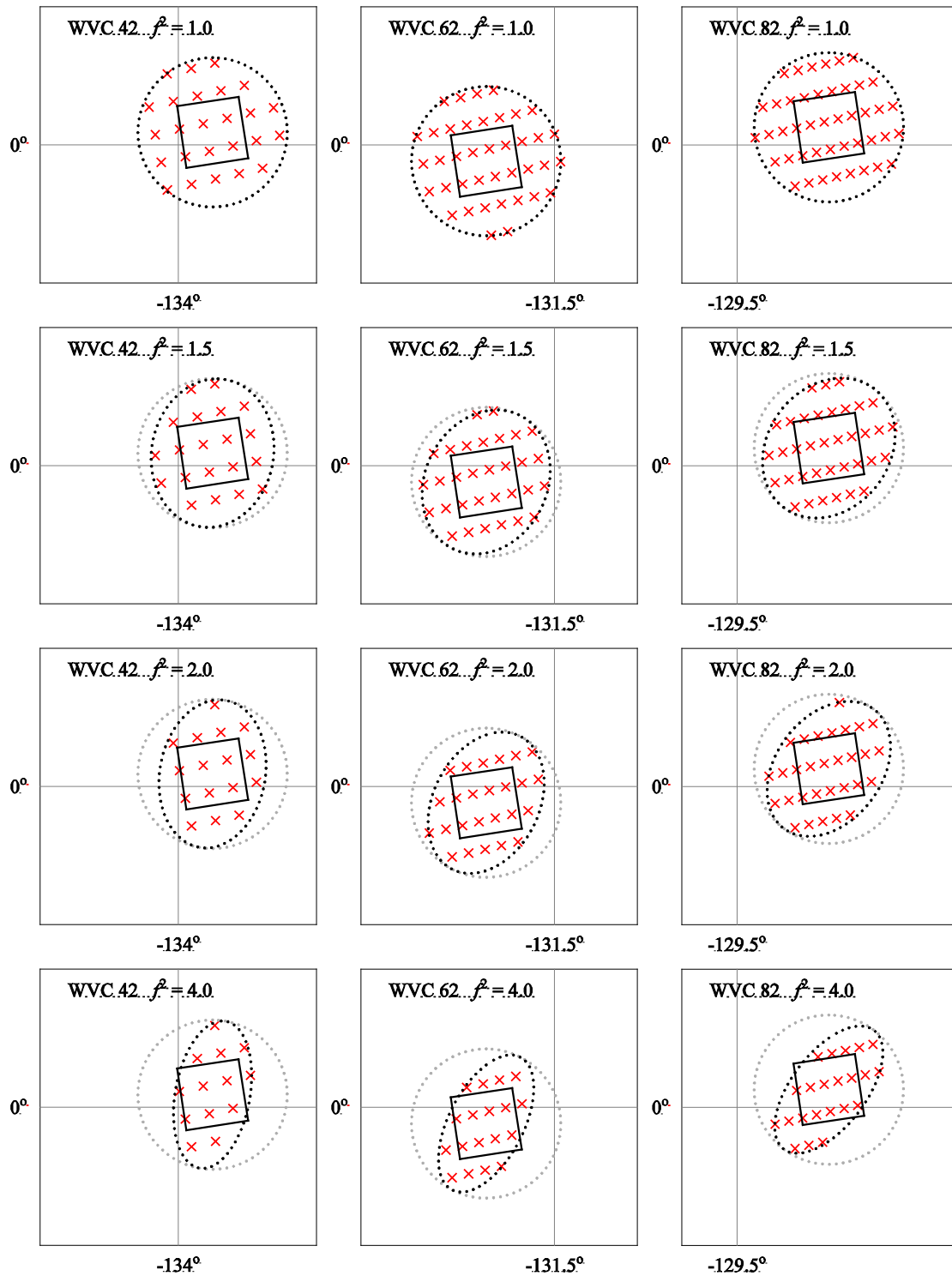**Figure 6.1** Mid beam CSRF for various choices of the shape of the aggregation area.

Figure 6.2 Centers of SRF's contributing to the CSRF's in figure 6.1.

Figure 6.1 shows the effect of varying f^2 on the mid beam CSRF for WVC 42 (smallest incidence angle), WVC 62 (intermediate incidence angle), and WVC 82 (largest incidence angle). Results are shown for f^2 equal to 1, 1.5, 2.0, and 4.0. For reasons of clarity, only the extension of the -1 dB, -2 dB and -3 dB regions are shown, the CRSF being normalised to 1 (0 dB). The black squares show the WVCs. The black dotted circles or ellipses show the aggregation areas, while the grey dotted circles for $f^2 > 1$ show the original circular aggregation area for reference.

Figure 6.1 shows that the mid beam CSRF gets a more irregular shape at the -3 dB level when increasing the eccentricity of the aggregation area, while the shape at low incidence angle (WVC 42) is hardly improved.

Figure 6.2 shows the centers of the SRF's contributing to the CSRF's in figure 6.1. Note that the number of contributing SRF's decreases as f^2 increases. For $f^2 = 4$ the number is about half of that for $f^2 = 1$. This implies that the CSRF is more noisy. Note also that the center of the aggregation area is not symmetrically located with respect to the SRF centers. This causes the irregular shape at large f^2.

6.3   Center of the aggregation area

The results of the previous section show that the position of the center of the aggregation area determines whether or not the contributing SRF's are symmetrically distributed. Therefore four alternative possibilities for shifting the center of the aggregation area are considered:

- M0   to the position of the SRF center closest to the WVC center;

- M4   to the middle of the four SRF centers closest to the WVC center;

- MA   to the middle of the two SRF centers in the along-track direction closest to the WVC center;

- MX   to the middle of the two SRF centers in the cross-track direction closest to the WVC center.

Figure 6.3 shows the resulting CSRF's for the mid beam with a circular aggregation area (black dotted). The WVC (black box) and the aggregation area are plotted at their original position.

The choices M0 and MX give the best results for WVC 82, though comparison with the original CSRF (figure 6.1, upper right hand panel) shows little improvement. The choice MX

gives the best result for WVC 42: the CSRF has become less elongated than the corresponding one in figure 6.1.

Figure 6.4 shows the centers of the SRF's contributing to the CSRF's in figure 6.3. Note that for WVC 42 only choice MX yields a symmetrical pattern. This is more or less accidental, because the SRF centers are not distributed uniformly over the Earth's surface. They are uniform in range, but the projection of range on the Earth's surface causes varying density of SRF's, the strongest effects being at low incidence angles.

This is corroborated by figures 6.5 and 6.6 that show results for a strongly elliptical aggregation area ($f^2 = 4$). Figure 6.6 shows that the sampling at WVC 42 is much more symmetric, because the long axis of the aggregation area is almost perpendicular to the range direction. However, the limited number of SRF's contributing to the CSRF causes irregular shapes as visible from figure 6.5.

This implies that in particular for low incidence angles it would probably more beneficial to define the aggregation area in range coordinates than in ground coordinates.
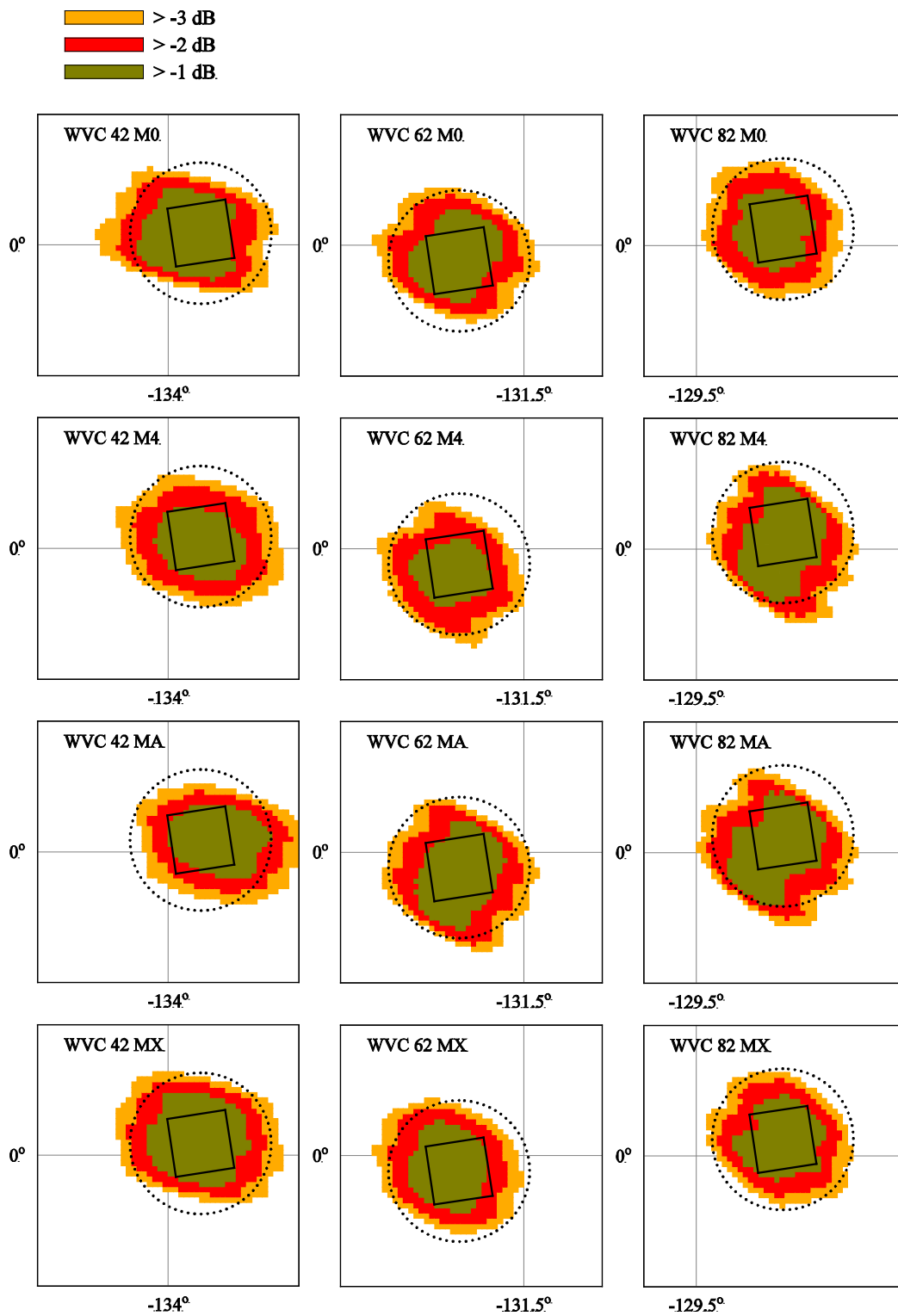
Figure 6.3 Mid beam CSRF for various choices for the center of the aggregation area.
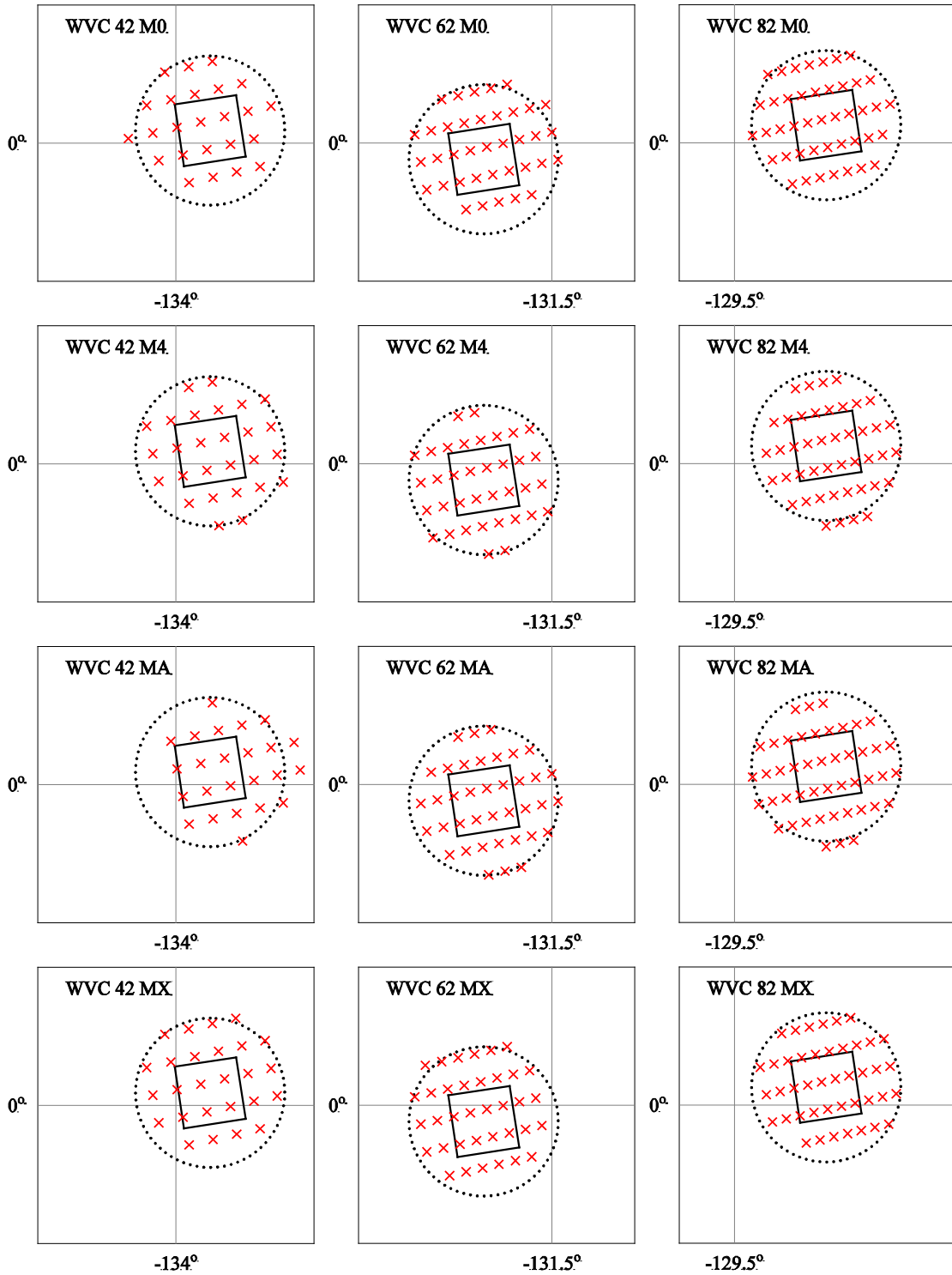
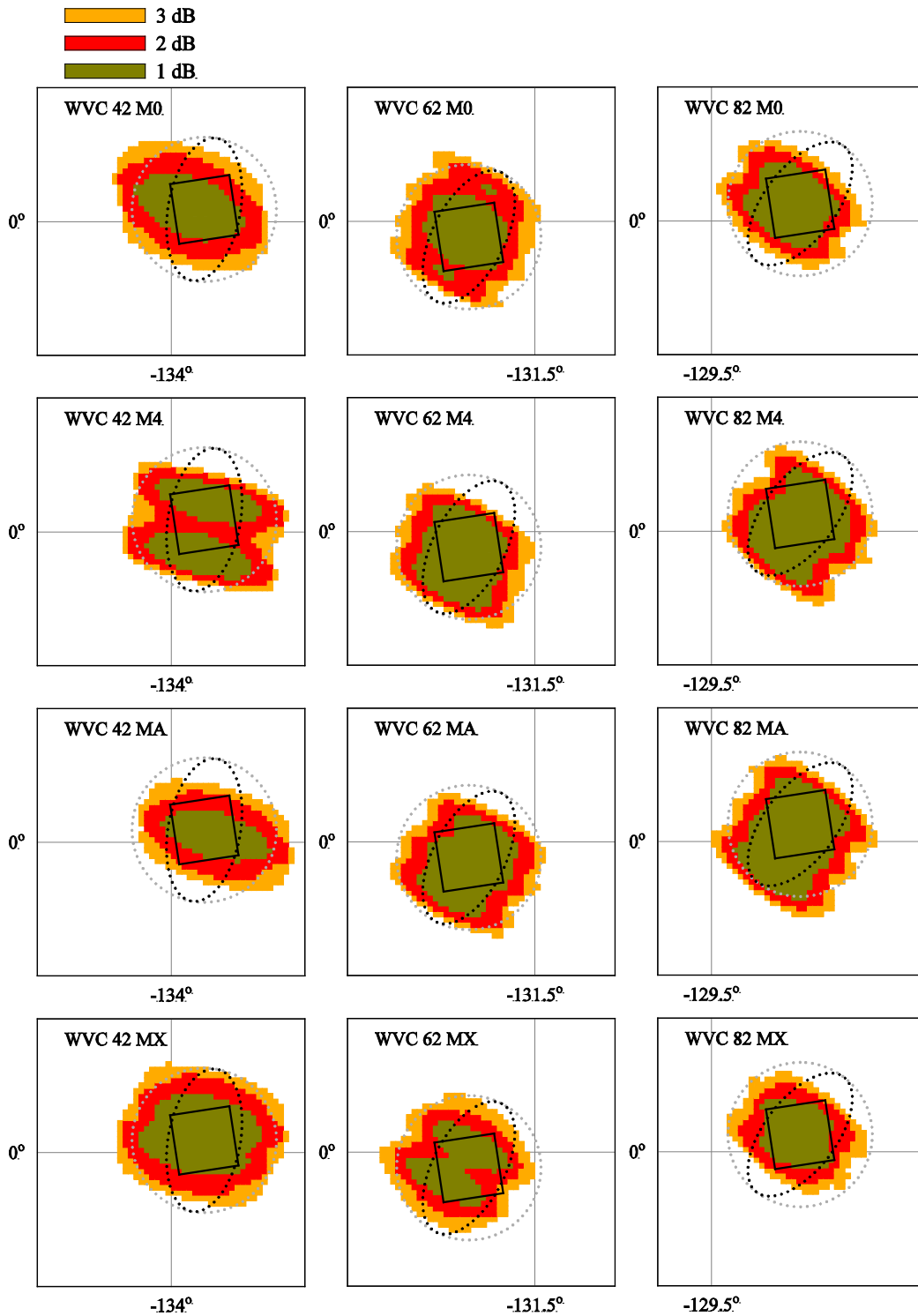**Figure 6.4** SRF's contributing to the CSRF's in figure 6.3.

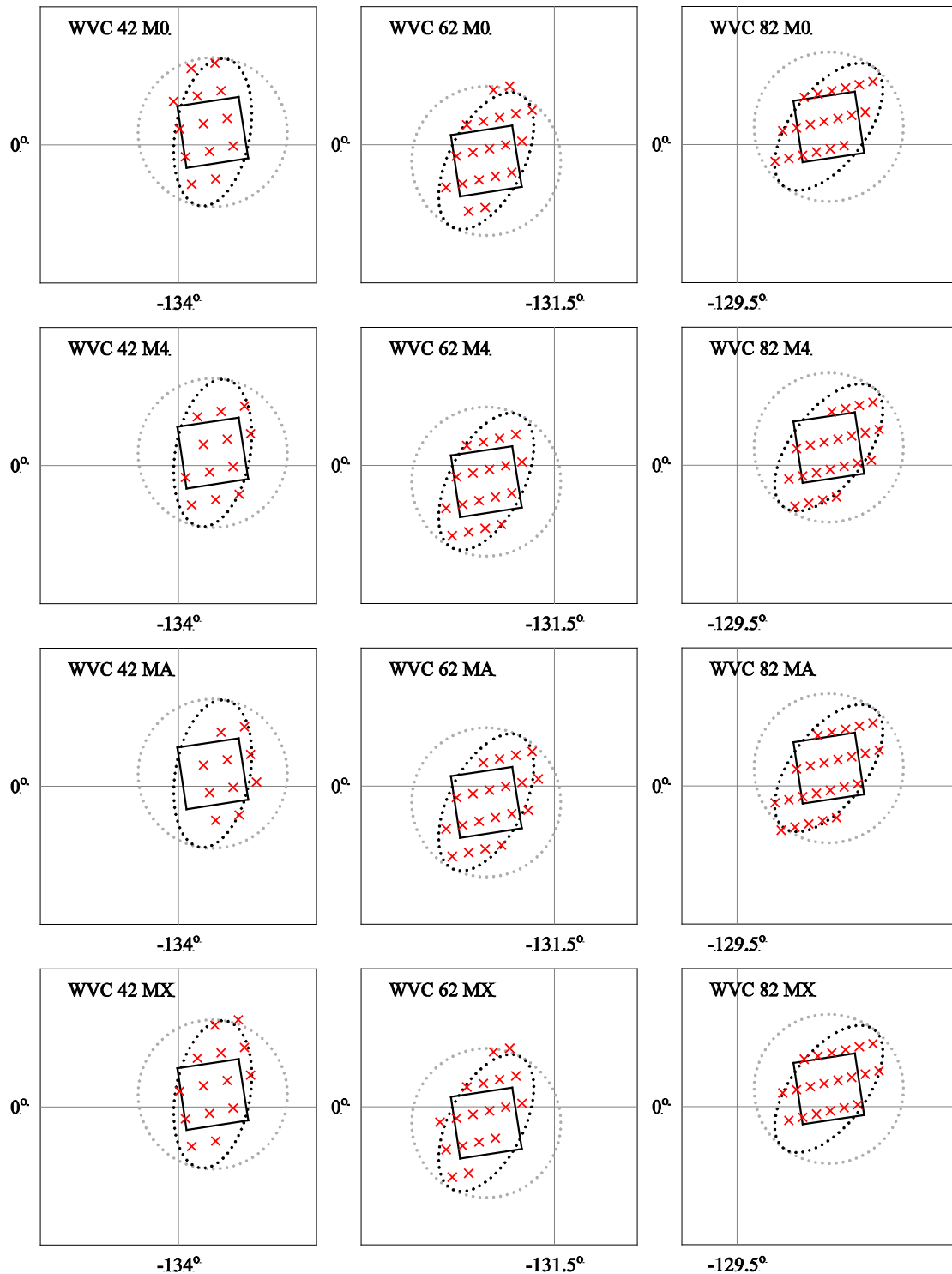**Figure 6.5** As figure 6.3, but for an elliptical aggregation area.

Figure 6.6 As figure 6.4, but for an elliptical aggregation area.

7 Concluding remarks

7.1 Beta user experiences

Four beta users obtained preliminary ASCAT-6.25 data sets:

- M. Bourassa and A. Hazelton (Florida State University, USA), for studying hurricanes Bill (2009), Earl (2010), and Irene (2013). A student's report by A. Hazelton showed that the ASCAT-6.25 winds were of good quality in terms of fine scale spatial boundaries, though ASCAT saturates for winds above 40 m/s. This is a consequence of the fact that ASCAT operates in C-band at VV polarization.

- A. Horvath (Rutherford Appleton Laboratory, UK), for studying von Karman vortices behind the wakes of isles. ASCAT-coastal and ASCAT-6.25 winds were compared with MISR cloud motion winds (MISR is an optical instrument viewing the Earth from nine different directions). It was found that ASCAT-6.25 and ASCAT-coastal were the only datasets that could 'validate' the experimental (4.4-km) MISR wind retrievals. Given that MISR retrieves cloud-level winds while ASCAT gives surface winds and also considering the ~1 hour time difference between the satellite overpasses during which the vortex street evolved a bit, the agreement between MISR and ASCAT turned out to be very good. ASCAT-6.25 also compared well with MISR in the finer details of the wind field. Also some differences were found that may be due to ASCAT ambiguity removal errors. See also *Nunalee et al.* [2015].

- M. Kuzmić (Ruder Bošković Institute, Croatia), for studying cold air outbreaks over the Adriatic Sea (Bora winds). However, the land/sea mask was found too restrictive to get any wind information between the isles off the Croatian coast. This can only be solved if the land/sea mask is improved, which is currently being studied by EUMETSAT.

- I. Monteiro (Instituto Português do Mar e da Atmosfera, Portugal), for studying coastal jets off the Iberian coast. Compared to the ASCAT-coastal product at 12.5 km, the ASCAT-6.25 product shows more detail in the coastal jets, in particular sharper and higher maxima in wind speed. Further validation activities were discussed during a NWPSAF Visiting Scientist mission to KNMI in 2015. See [*Monteiro et al.*, 2015] for more details.

7.2 User guidance

At this moment the Ocean and Sea Ice Satellite Application Facility (OSISAF) does not foresee operational NRT processing and dissemination of the ASCAT-6.25 product, because the user community for such a product is expected to be quite small. The main use of ASCAT-6.25 is foreseen for process studies like the ones listed in the previous paragraph.

This implies that potential users have to do their own processing using version 2.4 of the ASCAT Wind Data Processor (AWDP), to be released late 2015, using EUMETSAT archived L1B full resolution files and NWP forecasts. The Visiting Scientist mission of I. Monteiro made clear that a better description of how to operate AWDP in the User Manual is needed. From the current description the meaning of the command line arguments in AWDP is not clear enough. This has been solved in version 2.5 of the User manual, which contains an extra paragraph on ASCAT-6.25 processing with some test data.

7.3 Conclusions

In this report the new ASCAT-6.25 product is introduced and studied. The procedure for calculating the MLE normalization tables is given in detail.

Compared to the ASCAT-coastal product, the ASCAT-6.25 product shows more detail. This is indicated by the cumulative spatial response functions (CSRF) shown in figures 5.5 and 5.6, and has been confirmed by various beta users of the product. The ASCAT-6.25 product is also noisier than the ASCAT-coastal product, as becomes clear from buoy comparisons and a spatial variance analysis that has been developed for this purpose (see chapter 5 and Appendix F). An averaging radius of 7.5 km for the ASCAT-6.25 product is the optimum between increased resolution and increased noise due to a limited number of full resolution samples. This makes the ASCAT-6.25 product a downscaled version (by a factor of two) of the ASCAT-coastal product.

The sampling strategy for regridding the full resolution radar cross sections becomes critical for ASCAT-6.25, especially for the mid beam antenna. Some experiments with elliptical aggregation areas to compensate for the elliptical shape of the spatial reponse (see chapter 7) were unsuccessful. Another possibility is to define the ASCAT grid relative to the mid beam antenna pattern. This will be the subject of a separate study.

ASCAT-6.25 is more noisy than ASCAT-coastal. For Ku band scatterometers 2DVAR in combination with the Multiple Solution Scheme (MSS) proved beneficial to reduce the noise. This may also be the case for ASCAT-6.25, notably under extreme wind conditions. This also

The EUMETSAT Network of Satellite Application Facilities	**NWP SAF** Numerical Weather Prediction	ASCAT-6.25 validation

Doc ID : NWPSAF-KN-TV-009
Version : 1.0
Date : 19-05-2016

will be subject of a separate study. Figures 7.1 and 7.2 show as an example the centre of tropical cyclone Vong Fong (2014) processed on a 6.25 km grid. Figure 7.1 shows the standard result, where the centre is very noisy. Figure 7.2 shows the result obtained with MSS, taking 144 wind direction ambiguities into account. Now the cyclone structure is clearly visible, though perhaps too smoothly. It is interesting to note that some of the wind cells in figure 7.2 have a wind speed of 50 m/s - the end of the ASCAT scale!
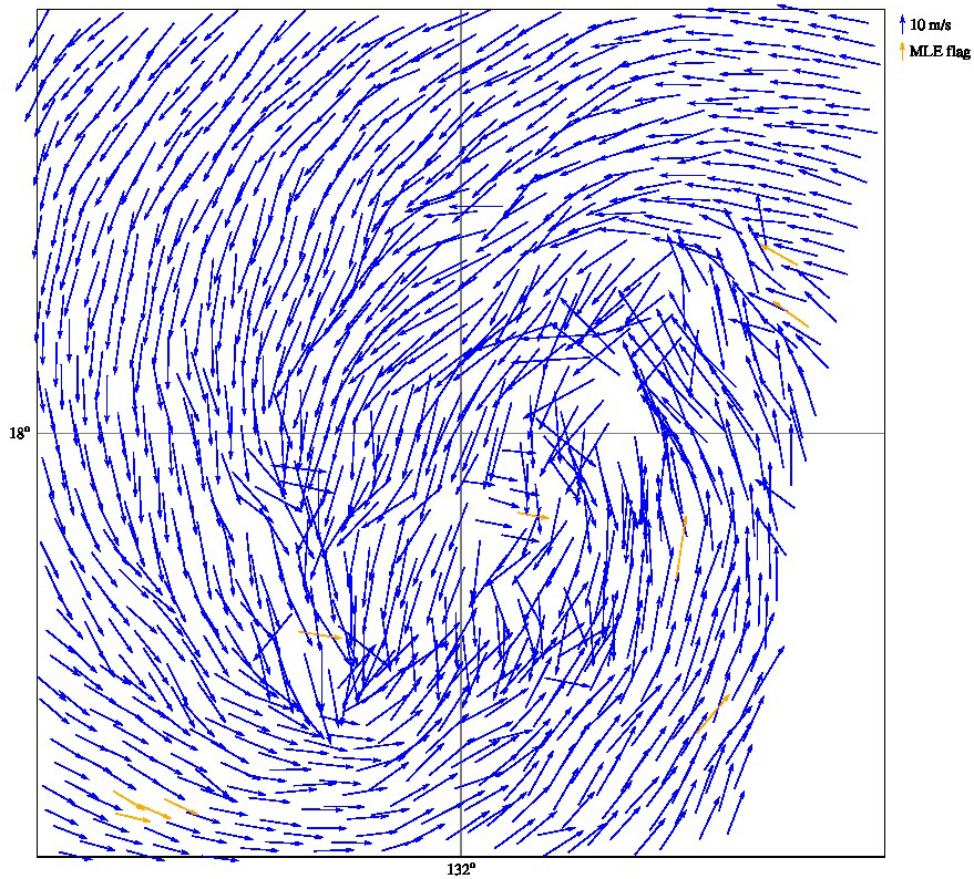

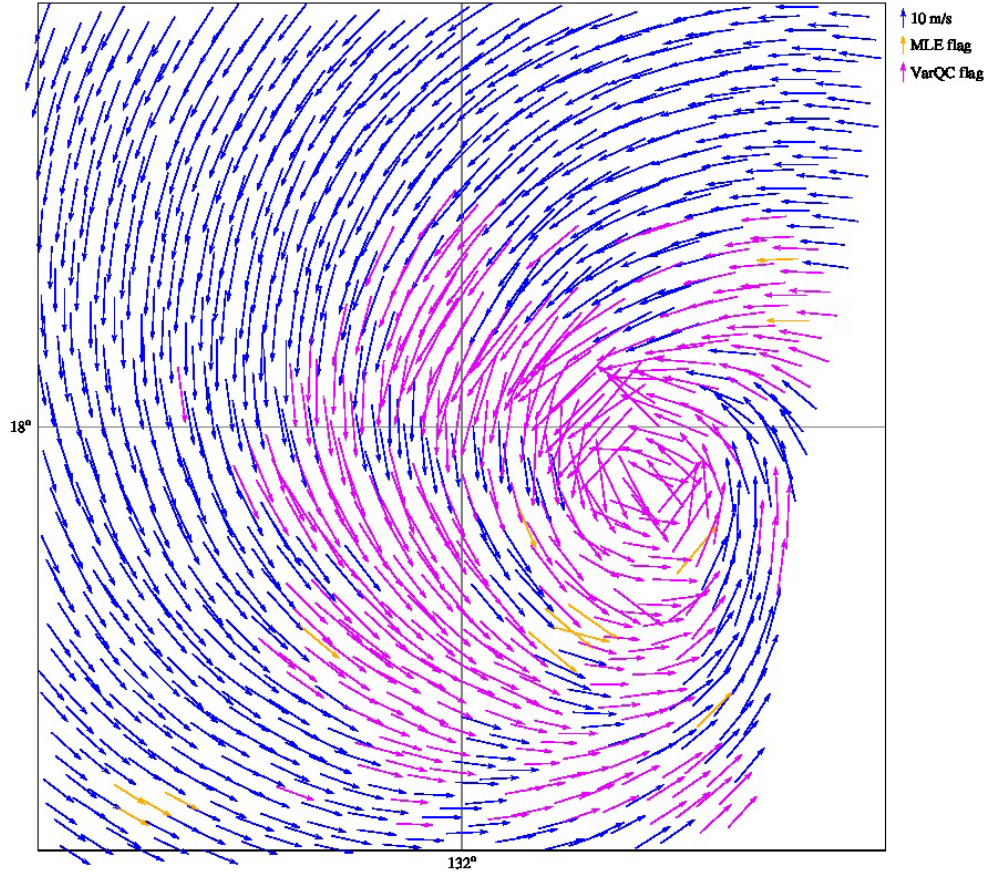**Figure 7.1** Centre of cyclone Fong Vong with standard ASCAT-6.25 processing

Figure 7.2 As figure 7.1, but processed with MSS.

Note

The wind fields in this chapter were calculated with the erroneous MLE normalization tables and QC threshold values based on the April-May 2013 data (see the note at the end of section 2.3). As a result, The MLE flagging (orange arrows) may not be entirely correct. However, for the purposes of this chapter this is not considered a serious drawback.

References

Lindsley, R.D., 2014
    ASCAT SRF code.
    Technical Report MERS 14-01, Brigham Young University, USA.
    http://www.mers.byu.edu/docs/reports/MERS1401.pdf

Lindsley, Richard, Craig Anderson, Julia Figa-Saldaña, and David Long, 2015.
    A parameterized ASCAT measurement spatial response function.
    IEEE Trans. Geosc. Rem. Sens., in review.

Monteiro, I., J. Vogelzang, and A. Stoffelen, 2015.
    ASCAT-6.25 validation on coastal jets.
    Report NWPSAF-KN-VS-015.
    https://nwpsaf.eu/vs_reports/nwpsaf-kn-vs-015.pdf

Nunalee, C.G., Á. Horváth, and S. Basu, 2015.
    High-resolution numerical modeling of mesoscale island wakes and sensitivity to
    static topographic relief data.
    Geosci. Model Dev., 8, 2645–2653. doi: 10.5194/gmd-8-2645-2015.

Vogelzang, J., G.P. King, and A. Stoffelen, 2015.
    Spatial variances and their relation to spectra and second-order structure functions.
    J. Geophys. Res. 120. doi: 10.1002/2014JC010239.

Williams, E., 2011
    Aviation formulary V1.46
    http://williams.best.vwh.net/avform.htm

Yates, F., 1948
    Systematic sampling.
    Phil. Trans. Royal Soc., **A241**, 345-377. doi: 10.1098/rsta.1948.0023.

Appendix A   calc_geophys_kp.F90

Source code of the program calc_geophys_kp used to calculate the ASCAT-6.25 geophysical

noise from the geophysical noise tables for ASCAT-25 and ASCAT-12.5.

```fortran
  program calc_geophys_kp
!
! Calculate geophysical noise table

  integer             :: n
  character(len=256)  :: table_250,table_125,table_063
  real                :: kp1,kp2,kp3
  real                :: ratio
  real                :: min_ratio,max_ratio
  integer             :: io1,io2

!
! Set input


table_250='/usr/people/vogelzan/genscat/inversion/ascat_25000_geoph_kp_vs_speed_and_in
c_ang.asc'

table_125='/usr/people/vogelzan/genscat/inversion/ascat_12500_geoph_kp_vs_speed_and_in
c_ang.asc'

table_063='/usr/people/vogelzan/genscat/inversion/ascat_6250_geoph_kp_vs_speed_and_inc
_ang.asc'

!
! Read tables for 25 km and 12.5 km, calculate ratio, write table for 6.25 km

  open(31 , file=table_250)
  open(32 , file=table_125)
  open(33 , file=table_063)
  n = 0

  write (*,*) 'program calc_geophys_kp'
  write (*,*) ' '
  write (*,*) '    ASCAT-25  ASCAT-12.5      ratio  ASCAT-6.25'
  write (*,*) '-----------------------------------------------'

  readloop: do
    read (31,*,iostat=io1) kp1
    read (32,*,iostat=io2) kp2

    if (io1 /= io2) then
      write (*,*) 'ERROR in program calc_geophys_kp: ' &
                  'input tables have different length'
      stop
    end if

    if (io1 /= 0) exit readloop

    n = n + 1
    ratio = kp2/kp1
    if (n == 1) then
      min_ratio = ratio
      max_ratio = ratio
    else
      if (ratio < min_ratio) min_ratio = ratio
      if (ratio > max_ratio) max_ratio = ratio
    end if
    kp3 = ratio*kp2

    write (*,'(4f12.8)') kp1,kp2,ratio,kp3
    write (33,'(f10.8)') kp3
  enddo readloop

  close(31)
```

```
close(32)
close(33)

write (*,*) ''
write (*,*) 'minimum ratio',min_ratio
write (*,*) 'maximum ratio',max_ratio

end program calc_geophys_kp
```

Appendix B   calc_mean_mle.F90

Source code of the FORTRAN program calc_mean_mle.F90 for calculating the ASCAT-6.25

mean MLE values per WVC.

```fortran
  program calc_mean_mles
  implicit none

  integer                :: narg
  integer, parameter      :: nwvc = 162
  integer, dimension(nwvc) :: mean_mle_cnt(nwvc)
  real, dimension(nwvc)    :: mean_mle(nwvc)
  integer                :: io,inode
  real                   :: conedist
  character(len=255)      :: infile

! Inintialise
  do inode = 1, nwvc
    mean_mle_cnt(inode) = 0
    mean_mle(inode) = 0.0
  enddo

! Handle command line arguments, read input file
  narg = iargc()
  if (narg /= 1) then
    write(*,*) ' '
    write(*,*) 'Usage: calc_mean_mles <input file>'
    write(*,*) ' '
    stop
  end if

  call getarg(1,infile)
  open(30,FILE=infile)

! read input data and put data in bins
  readloop: do
    read(30,*, iostat=io) inode,conedist
    if (io /= 0) exit readloop
    mean_mle(inode) = mean_mle(inode) + conedist
    mean_mle_cnt(inode) = mean_mle_cnt(inode) + 1
  enddo readloop

  close(30)

! Calculate and write mean values
  do inode = 1, nwvc
    if (mean_mle_cnt(inode) .gt. 0) then
      mean_mle(inode) = mean_mle(inode) / real(mean_mle_cnt(inode))
!!      write(*,*) inode, mean_mle(inode)
      write(*,*) mean_mle(inode)
    endif
  enddo

  end program calc_mean_mles
```

Appendix C   calc_rejection_rate.F90

Source code of the program calc_rejection_rate used to calculate the ASCAT-6.25 MLE rejection rate.

```fortran
  program calc_rejection_rate

  implicit none

  integer            :: narg
  integer            :: irej
  integer            :: nrej,ntot
  integer            :: io
  character(len=255) :: infile

! Inintialise
  nrej = 0
  ntot = 0

! Handle command line arguments, read input file
  narg = iargc()
  if (narg /= 1) then
    write(*,*) ' '
    write(*,*) 'Usage: calc_rejection_rate <input file>'
    write(*,*) ' '
    stop
  end if

  call getarg(1,infile)
  open(30,FILE=infile)

! read input data and put data in bins
  readloop: do
    read(30,*, iostat=io) irej
    if (io /= 0) exit readloop
    ntot=ntot + 1
    if (irej == 1) nrej=nrej + 1
  enddo readloop

  close(30)

! Calculate and write rejection rate
  write (*,*) "total number of points",ntot
  write (*,*) "number of rejections  ",nrej
  write (*,*) "rejection rate (in %) ",100.0*real(nrej)/real(ntot)

  end program calc_rejection_rate
```

Appendix D
calc_mle_normalisation_table.F90

Source code of the program calc_mle_normalisation_table used to calculate the ASCAT-6.25

MLE normalisation table.

```fortran
  program calc_mle_normalisation_table

  implicit none

  integer                 :: narg
  real                    :: mle1,mle2
  integer                 :: io1,io2,inode
  character(len=255)      :: in1,in2

! Initialise
  inode=0

! Handle command line arguments, read input file
  narg = iargc()
  if (narg /= 2) then
    write(*,*) ' '
    write(*,*) 'Usage: calc_mean_mles <result_step_1  result_step_2>'
    write(*,*) ' '
    stop
  end if

  call getarg(1,in1)
  call getarg(2,in2)
  open(31,FILE=in1)
  open(32,FILE=in2)

! read input data and multiply mle values, write output
  readloop: do
    read(31,*, iostat = io1) mle1
    read(32,*, iostat = io2) mle2
    inode = inode + 1
    if (io1 /= io2) then
      write (*,*) 'ERROR in calc_mle_normalisation_table at node',inode
      write (*,*) 'Illegal value in one of the input files or input files differ in
length'
      stop
    end if
    if (io1 /= 0) exit readloop
    write (*,*) mle1*mle2
  enddo readloop

  close(31)
  close(32)

  end program calc_mle_normalisation_table
```

Appendix E   calc_qc_threshold.F90

Source code of the program calc_qc_threshold used to calculate the ASCAT-6.25 MLE QC thresholds.

```fortran
  program calc_qc_threshold

  implicit none

  integer                  :: narg
  real                     :: mle
  integer                  :: io,inode
  character(len=255)       :: in

! Initialise
  inode=0

! Handle command line arguments, read input file
  narg = iargc()
  if (narg /= 1) then
    write(*,*) ' '
    write(*,*) 'Usage: calc_qc_threshold <result_step_2>'
    write(*,*) ' '
    stop
  end if

  call getarg(1,in)
  open(31,FILE=in)

! read input data and mute qc threshold, write output
  readloop: do
    read(31,*, iostat = io) mle
    inode = inode + 1
    if (io /= 0) exit readloop
    write (*,*) 18.45/mle
  enddo readloop

  close(31)

  end program calc_qc_threshold
```

Appendix F   Error analysis

Definitions

Suppose we have a dataset $\{u_i\} = \{u(r_i)\}$ with $r_i = i\Delta r, i = 0,1,2,\cdots,n$. Suppose further that the data contain noise, so that

$$u_i = s_i + \varepsilon_i \quad ,$$ (F.1)

with s_i the pure signal and ε_i the noise. The increment $\delta_{i;j} = u_i - u_{i+j}$ can be written as

$$\delta_{i;j} = (s_i - s_{i+j}) + (\varepsilon_i - \varepsilon_{i+j}) \quad ,$$ (F.2)

and its square as

$$\delta_{i;j}^2 = (s_i - s_{i+j})^2 + (\varepsilon_i - \varepsilon_{i+j})^2 + 2(s_i - s_{i+j})(\varepsilon_i - \varepsilon_{i+j}) \quad .$$ (F.3)

Now

$$D_j = \left\langle \delta_{i;j}^2 \right\rangle \quad ,$$ (F.4)

where the brackets $\langle\ \rangle$ denote averaging over all values of i. From (F.3) and (F.4) one obtains

$$D_j = D_j^{(S)} + D_j^{(N)} \quad ,$$ (F.5)

where $D_j^{(S)}$ stands for the signal part of the structure function and $D_j^{(N)}$ for the noise part, given by, respectively,

$$D_j^{(S)} = \left\langle (s_i - s_{i+j})^2 \right\rangle \quad ,$$ (F.6)

$$D_j^{(N)} = \left\langle (\varepsilon_i - \varepsilon_{i+j})^2 \right\rangle = 2\sigma^2(1 - \rho_j) \quad ,$$ (F.7)

with $\sigma^2 = \left\langle \varepsilon_i^2 \right\rangle = \left\langle \varepsilon_{i+j}^2 \right\rangle$ the noise variance and $\rho_j = \left\langle \varepsilon_i \varepsilon_{i+j} \right\rangle$ the noise autocorrelation. Further it has been assumed that the noise is not correlated with the signal strength, so that $\left\langle (s_i - s_{i+j})(\varepsilon_i - \varepsilon_{i+j}) \right\rangle = 0$. For scatterometer wind components (u,v) or (l,t) this assumption is justified.

The spatial variance V_j is defined by *Vogelzang et al.* [2013]. It is related to the second-order structure function by the Yates relation [*Yates,* 1948]

$$V_j = \frac{1}{(j+1)^2} \sum_{l=1}^{j} (j+1-l) D_l \quad . \tag{F.8}$$

Since the relation between spatial variance and second-order structure function is linear, also the spatial variance can be split in a signal part and a noise part, $V_j = V_j^{(S)} + V_j^{(N)}$, with

$$V_j^{(S)} = \frac{1}{(j+1)^2} \sum_{l=1}^{j} (j+1-l) D_l^{(s)} \quad , \tag{F.9}$$

$$V_j^{(N)} = \frac{2\sigma^2}{(j+1)^2} \sum_{l=1}^{j} (j+1-l)(1-\rho_l) \quad . \tag{F.10}$$

Uncorrelated noise

If the noise is uncorrelated, so $\rho_j = 0$ for all $j > 0$, the noise contribution to the structure function, (F.7), reduces to

$$D_j^{(N)} = 2\sigma^2 \quad . \tag{F.11}$$

Note that it becomes independent of the lag j. The noise contribution to the spatial variance, (F.10), becomes

$$V_j^{(N)} = \frac{2\sigma^2}{(j+1)^2} \sum_{l=1}^{j} (j+1-l) = \frac{j+2}{j+1}\sigma^2 \quad . \tag{F.12}$$

Now the noise contribution does depend on the lag. For lag 1 we have $V_1^{(N)} = \frac{3}{2}\sigma^2$ and for lag 2 we have $V_2^{(N)} = \frac{4}{3}\sigma^2$. For very large lag numbers the noise contribution approaches σ^2.

This is illustrated in figure F.1 using data from a fractional Brownian motion (FBM) process with exponent 2/3. The curves were obtained from a single sample of 2^{20} points. The solid curves are without additional noise, so these represent the signal part of the statistics. The dotted curves have uncorrelated Gaussian noise included with $\sigma = 1.0$.

The red curves show the second-order structure functions D_j, the blue curves the spatial variances V_j, and the purple curves the derivatives of the spatial variances

$$\frac{dV(r)}{dr} = \frac{V_j - V_{j-1}}{\Delta r} \quad , \tag{F.13}$$

with $V_0 = 0$ and $\Delta r = 1$ km. The latter value is important for the scaling of the derivative only.

The upper left panel shows the second-order structure function and the spatial variance as a function of lag. Addition of noise shifts the curves upward with 2 m^2/s^2 for the second-order structure function and 1 m^2/s^2 for the spatial variance.

The upper right panel shows the same curves as the upper left panel, but now on a double logarithmic scale. In the absence of noise the second-order structure function and the spatial variance are straight lines with slope 2/3, indicating a $r^{2/3}$ behaviour. Addition of noise flattens the curves for small lags. This effect is more pronounced for the structure function than for the spatial variance, because the noise contribution of the spatial variance depends on lag, see (F.12).
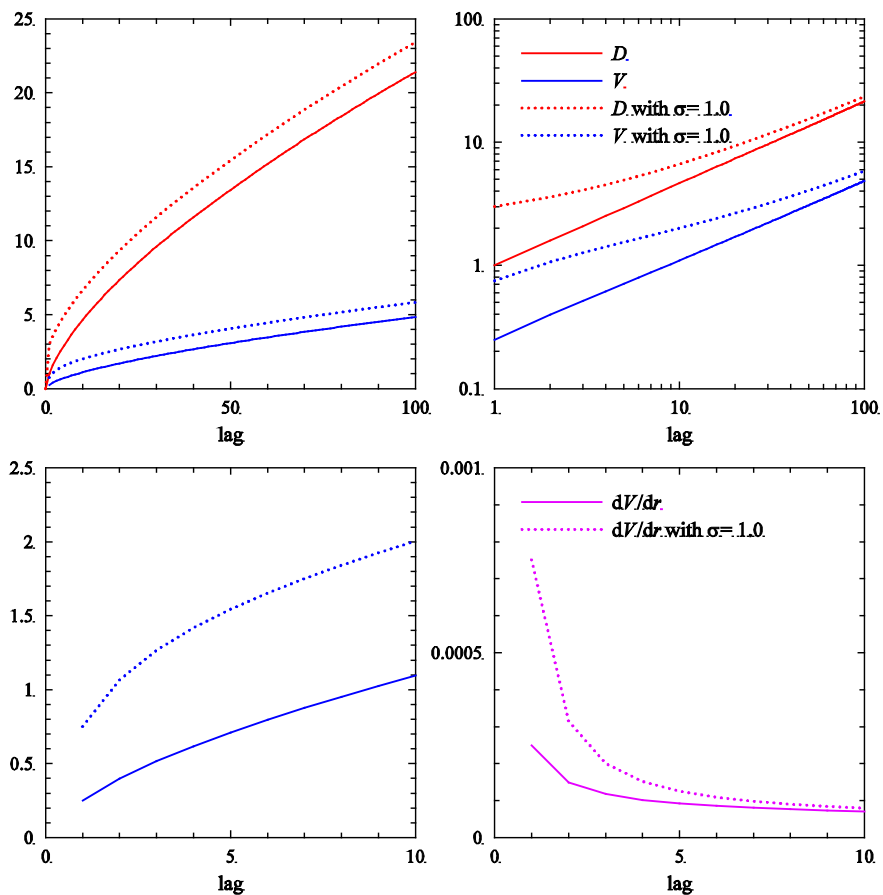
Figure F.1 Second-order structure functions (red curves), spatial variances (blue curves), and derivatives of spatial variances (purple curves) for simulated fractional Brownian motion data with (dotted) and without (solid) Gaussian uncorrelated noise.

The lower left panel of figure F.1 shows a detail of the spatial variance at small lags, while the lower right panel shows its derivative. This plot shows the effect of noise most clearly as a peak at small lags. From (F.12) and (F.13) one readily obtains

$$\Delta V_j^{(N)} = \frac{dV^{(N)}(r)}{dr}\bigg|_{r=r_j} = \frac{\sigma^2}{\Delta r}\frac{1}{j(j+1)} \quad . \tag{F.14}$$

For lag 1 the peak has size $\Delta V_1^{(N)} = \frac{1}{2}\sigma^2/\Delta r$ and for lag 2 $\Delta V_2^{(N)} = \frac{1}{6}\sigma^2/\Delta r$. The peak size drops rapidly with lag and has reduced to less than 1% of its maximum value for lag 10. Table F.1 gives the data used in figure F.1 for the first five lags. It also gives the noise peak value calculated from subtracting the noise free derivative from the noisy one and it compares with the theoretical result (F.14). All values are multiplied with 10^3, because the grid size is assumed to be 1 km.

r (km)	$\frac{dV}{dr}\times 10^3$ no noise	$\frac{dV}{dr}\times 10^3$ with noise	$\Delta V^{(N)}\times 10^3$	$(F.14)\times 10^3$
1.0	0.249624	0.751075	0.501451	0.500000
2.0	0.148671	0.315238	0.166567	0.166667
3.0	0.117552	0.200548	0.082996	0.083333
4.0	0.101891	0.151661	0.049770	0.050000
5.0	0.092132	0.125285	0.033126	0.033333

Table F.1 Noise peak comparison.

Table F.1 shows that $\Delta V_j^{(N)}$ obtained from the data matches the theoretical result up to about three decimal places. This means that spatial variances can be used to estimate noise if one of the following conditions are met:

1. the noise is uncorrelated;
2. the noise is correlated and the signal part is known from fit to a power law (or something else);
3. the noise is correlated and a reference signal without noise (or with strongly reduced noise) is available.

For the data in figure F.1 and table F.1 the noise variance would be estimated between 1.003 and 0.994 m²/s², which agrees very well with the actual value of 1 m²/s².

Correlated noise

Things become more complicated when the noise is correlated. If only the noise between neighbouring points is correlated, so $\rho_1 \neq 0$ and $\rho_j = 0$ for $j \geq 2$, the noise contribution to the second-order structure function, (F.7), becomes

$$D_j^{(N)} = \begin{cases} 2\sigma^2(1-\rho_1) & j = 1 \\ 2\sigma^2 & j \geq 2 \end{cases} . \tag{F.15}$$

From that the noise contribution to the spatial variance, (F.10), reads

$$\begin{aligned} V_j^{(N)} &= \frac{2\sigma^2}{(j+1)^2}\left[j(1-\rho_1) + \sum_{l=2}^{j} (j+1-l)(1-\rho_l) \right] = \\ &= \frac{2j}{(j+1)^2}\sigma^2(1-\rho_1) + \frac{j(j-1)}{(j+1)^2}\sigma^2 \quad . \end{aligned} \tag{F.16}$$

Note that the second term in (F.16) vanishes for $j = 1$.

The noise peak values in the derivative of the spatial variance become

$$\Delta V_j^{(N)} = \begin{cases} \dfrac{1}{2}(1-\rho_1)\dfrac{\sigma^2}{\Delta r} & , \quad j = 1 \\[2em] \left[\dfrac{2}{9} - \dfrac{1}{18}(1-\rho_1)\right]\dfrac{\sigma^2}{\Delta r} & , \quad j = 2 \\[2em] \left[\dfrac{(j-1)(3j+2)}{j^2(j+1)^2} - \dfrac{2(j^2-j-1)}{j^2(j+1)^2}(1-\rho_1)\right]\dfrac{\sigma^2}{\Delta r} & , \quad j \geq 3 \end{cases} . \tag{F.17}$$

Table F.2 gives the coefficient of $\sigma^2/\Delta r$ for uncorrelated and single correlated noise with $\rho_1 = 1/2$ for a few values of the lag.

j	uncorrelated noise	single correlated noise
1	1/2	1/4
2	1/6	7/36
3	1/12	17/144
4	1/20	31/400

5	1/30	49/900

Table F.2 Noise peak coefficients.

Note that for single correlated noise the noise peak at lag 1 is lower than that for uncorrelated noise, while those at lag 2 and 3 are higher. Therefore checking the height of the noise peak at various lag sizes may reveal if the noise is correlated or not. If the noise is not correlated, the peak heights decrease according to (F.14).

The general formula for correlated noise reads

$$
\begin{aligned}
\Delta V_j^{(N)} = \frac{V_j - V_{j-1}}{\Delta r} = \\
= \frac{2\sigma^2}{(j+1)^2 \Delta r} \sum_{l=1}^{j} (j+1-l)(1-\rho_l) - \frac{2\sigma^2}{j^2 \Delta r} \sum_{l=1}^{j-1} (j-l)(1-\rho_l) = \\
= \frac{\sigma^2}{\Delta r} \left[\frac{2}{(j+1)^2}(1-\rho_j) + \sum_{l=1}^{j-1} \left\{ \frac{2(j+1-l)}{(j+1)^2} - \frac{2(j-l)}{j^2} \right\}(1-\rho_l) \right] = \\
= \frac{\sigma^2}{\Delta r} \left[\frac{2}{(j+1)^2}(1-\rho_j) + \sum_{l=1}^{j-1} 2\frac{l(2j+1) - j(j+1)}{j^2(j+1)^2}(1-\rho_l) \right] .
\end{aligned}
\tag{F.18}
$$

The summation in (F.18) can be extended to $l = j$, and since $j(2j+1) - j(j+1) = j^2$ we have

$$
\Delta V_j^{(N)} = \frac{\sigma^2}{\Delta r} \sum_{l=1}^{j} 2\frac{l(2j+1) - j(j+1)}{j^2(j+1)^2}(1-\rho_l) .
\tag{F.19}
$$

Putting $R_j = 1 - \rho_j$, the first terms read explicitly

$$
\Delta V_1^{(N)} = \frac{\sigma^2}{\Delta r}\frac{R_1}{2} ,
\tag{F.20a}
$$

$$
\Delta V_2^{(N)} = \frac{\sigma^2}{\Delta r}\frac{4R_2 - R_1}{18} ,
\tag{F.20b}
$$

$$
\Delta V_3^{(N)} = \frac{\sigma^2}{\Delta r}\frac{9R_3 + 2R_2 - 5R_1}{72} ,
\tag{F.20c}
$$

$$
\Delta V_4^{(N)} = \frac{\sigma^2}{\Delta r}\frac{16R_4 + 7R_3 - 2R_2 - 11R_1}{200} ,
\tag{F.20d}
$$

$$\Delta V_5^{(N)} = \frac{\sigma^2}{\Delta r} \frac{25R_5 + 14R_4 + 3R_3 - 8R_2 - 19R_1}{450} \quad . \tag{F.20e}$$

Figure F.2 shows the structure functions, spatial variances, and derivatives of spatial variances for Brownian fractional motion with $p = 2/3$, similar to figure F.1. Besides the curves without noise (solid) and curves with uncorrelated Gaussian noise with unit standard deviation (dotted), figure F.2 also shows results for correlated noise with unit standard deviation. The correlation was introduced by taking uniformly weighted running averages of length 2 (dashed curves, labeled RA 2), length 3 (dot-dashed curves labeled RA 3), and length 5 (dot-dot-dashed curves labeled RA 5).

The differences are most clearly seen in the structure functions and spatial variances on a double logarithmic scale (upper right panel) and the derivatives of the spatial variances (lower right panel). Inclusion of error correlations flattens the noise peak at the lags over which the correlation extends. The structure functions with correlated and uncorrelated errors overlap for large lag numbers, since all curves have unit standard deviation. As a result, the structure functions with correlated errors assume an S-shape.

Inclusion of error correlations flattens and broadens the noise peak in the derivative of the spatial variance, as can be seen in the lower right panel of figure F.2.

Solution

Write

$$\Delta V_j^{(N)} = \frac{\sigma^2}{\Delta r} \sum_{l=1}^{j} c_{jl} R_l \quad , \tag{F.21}$$

where

$$c_{jl} = \begin{cases} 2\dfrac{l(2j+1) - j(j+1)}{j^2(j+1)^2} & , \quad l \le j \\ 0 & , \quad l > j \end{cases} \quad . \tag{F.22}$$

Suppose we have a set of values of $\Delta V_j^{(N)}$ for $j = 1, 2, \cdots, J$. Equation (F.21) defines a system of J equations with $J+1$ unknowns R_j, $j = 1, 2, \cdots, J$ and σ^2. First divide all equations by $\Delta V_1^{(N)}$ to eliminate σ^2 and Δr. This yields

$$\frac{\Delta V_j^{(N)}}{\Delta V_1^{(N)}} = \frac{\dfrac{\sigma^2}{\Delta r} \displaystyle\sum_{l=1}^{j} c_{jl} R_l}{\dfrac{\sigma^2}{\Delta r} c_{11} R_1} = \sum_{l=1}^{j} 2 c_{jl} \frac{R_l}{c_{11} R_1} \quad , \quad j = 2,3,\cdots,J \quad . \tag{F.23}$$
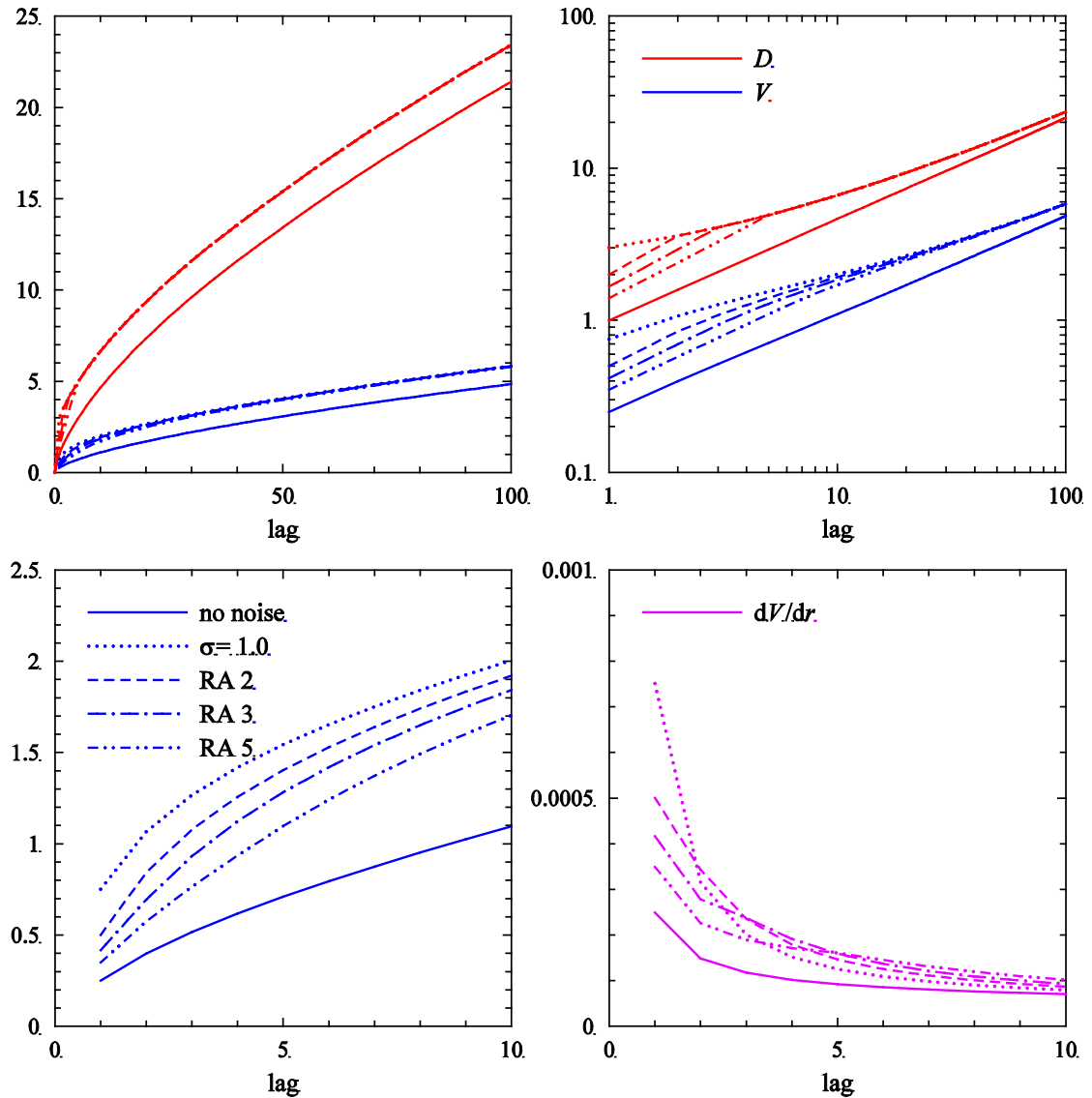
Figure F.2 Second-order structure functions (red curves), spatial variances (blue curves), and derivatives of spatial variances (purple curves) for simulated fractional Brownian motion data with various error types (see text).

Multiplying with $c_{11}R_1$ and rearranging terms yields

$$-c_{11}\frac{\Delta V_j^{(N)}}{\Delta V_1^{(N)}}R_1 + \sum_{l=1}^{j} c_{jl}R_l = 0 \quad , \quad j = 2, 3, \cdots, J \quad . \tag{F.24}$$

This is a system of $J-1$ equations with J unknowns. If we put $R_J = 0$ it reduces to a system of $J-1$ equations in $J-1$ unknowns $R_1, R_2, \cdots, R_{J-1}$. In matrix form it reads

$$
\begin{pmatrix}
c_{2,1} - c_{1,1}\Delta_2 & c_{2,2} & 0 & \cdots & 0 \\
c_{3,1} - c_{1,1}\Delta_3 & c_{3,2} & c_{3,3} & \cdots & 0 \\
\vdots & \vdots & \vdots & \ddots & \vdots \\
c_{J-1,1} - c_{1,1}\Delta_{J-1} & c_{J-1,2} & c_{J-1,3} & \cdots & c_{J-1,J-1} \\
c_{J,1} - c_{1,1}\Delta_J & c_{J,2} & c_{J,3} & \cdots & c_{J,J-1}
\end{pmatrix}
\begin{pmatrix}
R_1 \\ R_2 \\ \vdots \\ R_{J-2} \\ R_{J-1}
\end{pmatrix}
=
\begin{pmatrix}
0 \\ 0 \\ \vdots \\ 0 \\ -c_{J,J}
\end{pmatrix}
, \quad \text{(F.25)}
$$

where we have written $\Delta_j = \Delta V_j^{(N)} / \Delta V_1^{(N)}$. This system is easily triangularized and solved. The variance can be retrieved from

$$
\Delta V_1^{(N)} = \frac{\sigma^2}{\Delta r} c_{11} R_1 \quad \Leftrightarrow \quad \sigma^2 = \frac{\Delta r \Delta V_1^{(N)}}{c_{11} R_1} \quad . \tag{F.26}
$$

For uncorrelated noise we have $R_1 = 1$ and (F.26) reduces to $\sigma^2 = 2\Delta r \Delta V_1^{(N)}$ since $c_{11} = \frac{1}{2}$.

Example

As an example, consider the RA 5 results in figure F.3. Application of the formalism outlined above on these data gives the results listed in table F.3, where n stands for the number of lags taken into account. As reference dataset the results without errors were used. For $n = 1$ only the variance σ^2 can be retrieved; for $n > 1$ also $n - 1$ correlations can be found.

n	σ^2	ρ_1	ρ_2	ρ_3	ρ_4	ρ_5
1	0.199434	0.0	0.0	0.0	0.0	0.0
2	0.397647	0.498464	0.0	0.0	0.0	0.0
3	0.596088	0.665428	0.332906	0.0	0.0	0.0
4	0.794765	0.749065	0.499668	0.249983	0.0	0.0
5	0.994950	0.799554	0.600335	0.400887	0.201200	0.0
6	0.994996	0.799563	0.600354	0.400915	0.201237	0.000047
Exact	1.0	0.8	0.6	0.4	0.2	0.0

Table F.3 Error analysis results for fractional Brownian motion with equally weighted running average of length 5.

Table F.3 shows that the values for the variance and the correlation coefficients $\rho_j = 1 - R_j$ converge to the right values as n increases to 5 with an accuracy of about 0.005. This convergence occurs also when using real data with unknown number of correlation coefficients as in chapter 5, and can be used to estimate the number of nonzero correlation coefficients. For larger values of n the excess correlation coefficients are smaller than the

accuracy, consistent with zero value. Note that the variance is underestimated when an insufficient number of correlation coefficients is assumed ($n < 5$).

Limitations

So far, it has been assumed that the signal remains the same. In practical applications to scatterometer wind products, not only the noise but also the signal content will depend on the processing details. To get more feeling for these effects, figure F.3 shows the effect of running averaging with window lengths 2, 3 and 5 (dashed, dot-dashed and dot-dot-dashed curves, respectively) on the FBM signal without noise. The curves are to be compared with the solid curves, the dotted curves (FBM with Gaussian noise) is added for reference.

Figure F.3 shows that application of a running average lowers the second-order structure function, the spatial variance, and the derivative of the spatial variance. The effect of the running average on the FBM signal is to reduce the effective resolution. As a result, the structure function and the spatial variance show a steeper slope in double logarithmic plots (upper right panel of figure F.3). The plot of the derivative of the spatial variance (lower right panel of figure F.3) shows that the reduction is restricted to small lags, as expected. Nevertheless, the spatial variance itself and the second-order structure function are affected significantly at larger lags, because these are cumulative quantities.

Figure F.4 is similar to figure F.3, but now the running average is applied to the FBM signal plus Gaussian noise with unit standard deviation. Now the results at various window lengths are to be compared with the dotted curves. Note that for a window size of 3 or more (dot-dashed and dot-dot-dashed curves) the derivative of the spatial variance at lag 1 lies below the noise-free reference (solid curve). In these cases the solution scheme presented above will break down. Also, there is no alternative curve that lies below the other curves in order to act as reference.
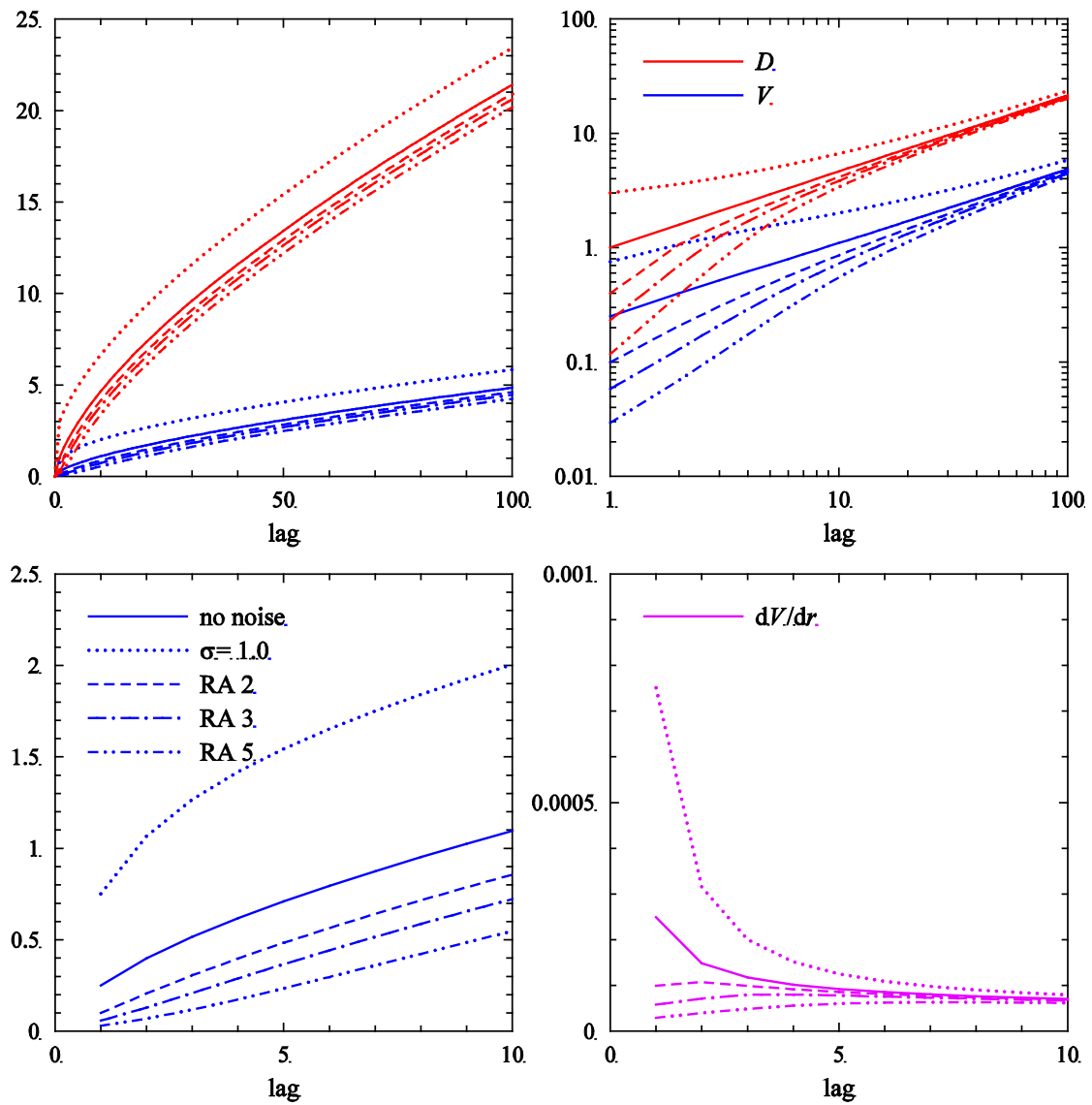
Figure F.3 Second-order structure functions (red curves), spatial variances (blue curves), and derivatives of spatial variances (purple curves) for simulated fractional Brownian motion data without noise and various running average window lengths (see text).
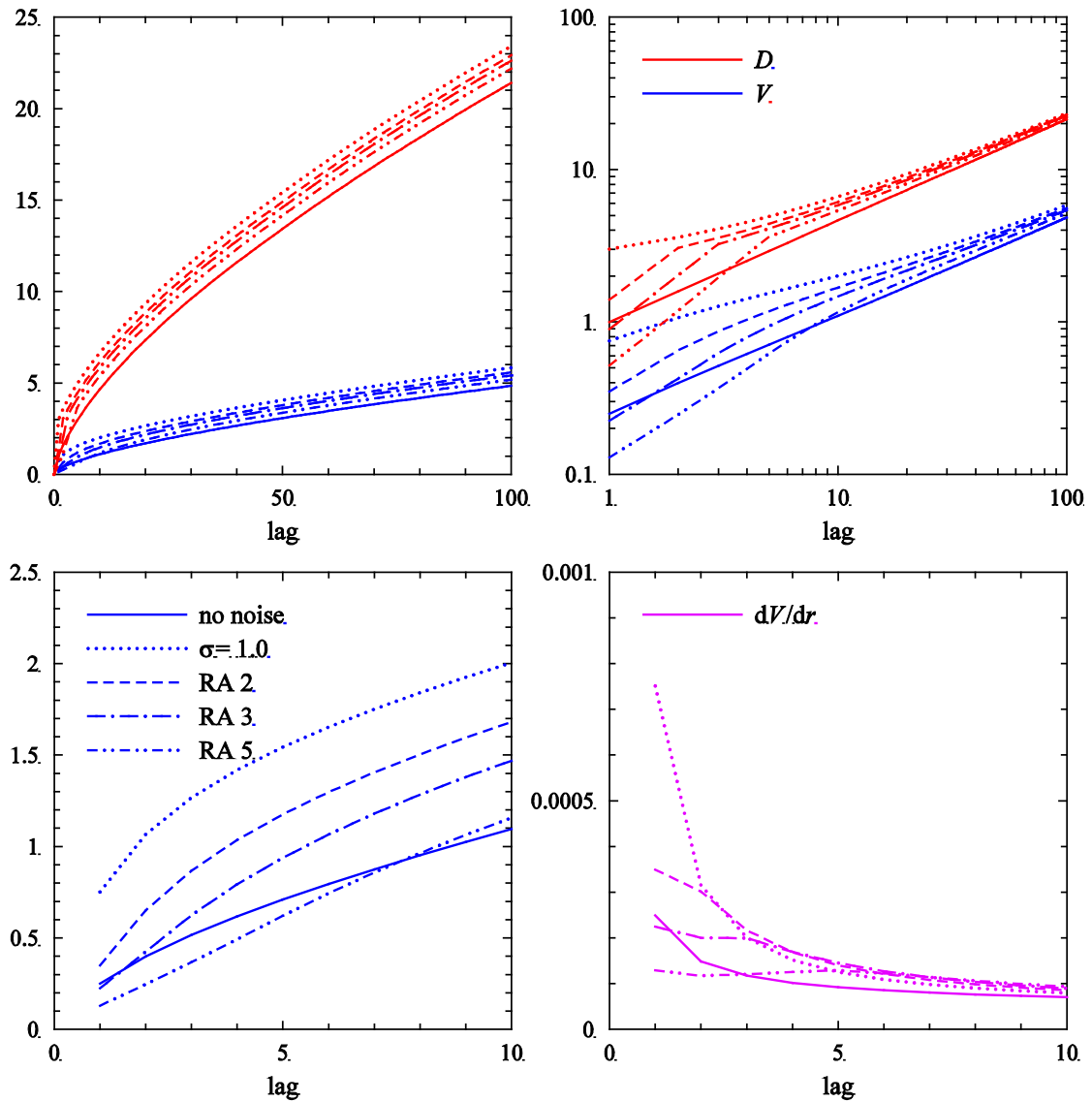
Figure F.4 Second-order structure functions (red curves), spatial variances (blue curves), and derivatives of spatial variances (purple curves) for simulated fractional Brownian motion data with unit variance Gaussian noise and various running average window lengths (see text).